

# Non-Coherent Over-the-Air Decentralized Gradient Descent

Nicolò Michelusi

**Abstract**—Implementing Decentralized Gradient Descent (DGD) in wireless systems is challenging due to noise, fading, and limited bandwidth, necessitating topology awareness, transmission scheduling, and the acquisition of channel state information (CSI) to mitigate interference and maintain reliable communications. These operations may result in substantial signaling overhead and scalability challenges in large networks lacking central coordination. This paper introduces a scalable DGD algorithm that eliminates the need for scheduling, topology information, or CSI (both average and instantaneous). At its core is a Non-Coherent Over-The-Air (NCOTA) consensus scheme that exploits a noisy energy superposition property of wireless channels. Nodes encode their local optimization signals into energy levels within an OFDM frame and transmit simultaneously, without coordination. The key insight is that the received energy equals, *on average*, the sum of the energies of the transmitted signals, scaled by their respective average channel gains, akin to a consensus step. This property enables unbiased consensus estimation, utilizing average channel gains as mixing weights, thereby removing the need for their explicit design or for CSI. Introducing a consensus stepsize mitigates consensus estimation errors due to energy fluctuations around their expected values. For strongly-convex problems, it is shown that the expected squared distance between the local and globally optimum models vanishes at a rate of  $\mathcal{O}(1/\sqrt{k})$  after  $k$  iterations, with suitable decreasing learning and consensus stepsizes. Extensions accommodate a broad class of fading models and frequency-selective channels. Numerical experiments on image classification demonstrate faster convergence in terms of running time compared to state-of-the-art schemes, especially in dense network scenarios.

## I. INTRODUCTION

Decentralized Gradient Descent (DGD) is a popular algorithm used for solving optimization problems across various domains such as remote sensing, distributed inference [3], estimation [4], multi-agent coordination [5], and machine learning (ML) [6]. Typically, in these applications,  $N$  devices with sensing, computation and wireless communication capabilities aim to find a global  $\mathbf{w}^* \in \mathbb{R}^d$ , solution of

$$\mathbf{w}^* = \arg \min_{\mathbf{w} \in \mathbb{R}^d} F(\mathbf{w}), \text{ where } F(\mathbf{w}) \triangleq \frac{1}{N} \sum_{i=1}^N f_i(\mathbf{w}), \quad \{\mathbf{P}\}$$

$f_i(\mathbf{w})$  is a local function only known to node  $i$ ,  $\mathbf{w}$  is a  $d$ -dimensional parameter, so that  $F(\mathbf{w})$  is the network-wide objective. For instance, in ML applications,  $f_i(\mathbf{w}) = \frac{1}{|\mathcal{D}_i|} \sum_{\xi \in \mathcal{D}_i} \phi(\xi; \mathbf{w})$  is the empirical loss over the local dataset  $\mathcal{D}_i$ , with loss function  $\phi(\xi; \mathbf{w})$  on the datapoint  $\xi$ . In distributed linear regression, each node measures  $\mathbf{w}^*$  via  $\mathbf{y}_i = \mathbf{A}_i \mathbf{w}^* + \mathbf{n}_i$  corrupted by noise  $\mathbf{n}_i$ , corresponding to the error metric  $f_i(\mathbf{w}) = \frac{1}{2} \|\mathbf{y}_i - \mathbf{A}_i \mathbf{w}\|_2^2$  for node  $i$  [4].

Federated learning (FL) solves  $\{\mathbf{P}\}$  based on a client-server architecture, in which the  $N$  devices (the clients) interact over multiple rounds with a parameter server (PS, such as a base station), acting as a model aggregator. Nevertheless, the FL architecture encounters several challenges in wireless scenarios: 1) devices far away from the PS (e.g., in rural areas), may suffer from severe path loss conditions and blockages [7]; 2) uplink communications to the PS may be a severe bottleneck when  $N$  is large, due to limited bandwidth [8]; 3) if the PS fails, e.g., due to a natural disaster, the whole system may break down. Therefore, in crucial scenarios like swarms of unmanned aerial vehicles (UAVs) in remote regions [9] or disaster response operations, solving  $\{\mathbf{P}\}$  in a fully decentralized way, without centralized coordination, is paramount [10].

A renowned algorithm solving  $\{\mathbf{P}\}$  in a fully decentralized fashion is *Decentralized Gradient Descent* (DGD) [11], [12] and its stochastic gradient variant [13]: each node ( $i$ ) owns a local copy  $\mathbf{w}_i \in \mathbb{R}^d$  of  $\mathbf{w}$  (its *state*), and transmits it to its neighbors in the network; upon receiving its neighbors' states, it then updates  $\mathbf{w}_i$  as a weighted average of the received signals (the consensus signal  $\mathbf{c}_i$ ), followed by a local gradient step, illustrated here as non-stochastic for clarity,

$$\mathbf{w}_i \leftarrow \mathbf{c}_i - \eta \nabla f_i(\mathbf{w}_i), \text{ with } \mathbf{c}_i = \sum_{j=1}^N \omega_{ij} \mathbf{w}_j. \quad \{\text{DGD}\}$$

Here,  $\omega_{ij}$  denotes a set of non-negative, symmetric ( $\omega_{ij} = \omega_{ji}$ ) mixing weights, such that  $\sum_{j=1}^N \omega_{ij} = 1$ , defined over a mesh network ( $\omega_{ij} = 0$  if  $i$  and  $j$  are not direct neighbors). These steps are repeated across the  $N$  nodes and over multiple iterations, until a desired convergence criterion or deadline are met. Yet, in wireless systems affected by noise, fading, and interference, reliably communicating  $\mathbf{w}_j$ , which is necessary to compute  $\mathbf{c}_i$ , introduces delays. For example, in a TDMA implementation of DGD, the  $N$  nodes broadcast their local state to their neighbors in pre-assigned time slots in a round-robin fashion. This strategy protects transmissions from mutual interference, thus facilitating reliable communications during the consensus phase. However, the time required to complete one DGD iteration scales proportionally with  $N$ . Consequently, with a large  $N$ , this scheme may complete only a few DGD iterations within a given deadline, resulting in poor convergence performance. Communication delays may be reduced by quantizing  $\mathbf{w}_j$  below machine precision [4], [14]–[17], or via non orthogonal transmissions [18], at the cost of errors introduced in the computation of  $\mathbf{c}_i$ .

Consequently, there is a tension between accurately computing  $\mathbf{c}_i$  and minimizing the communication delay of each DGD iteration. In fully decentralized wireless systems lacking centralized coordination, this tension is further exacerbated by the signaling overhead associated with tasks such as scheduling,

N. Michelusi is with the School of Electrical, Computer and Energy Engineering, Arizona State University. Part of this work appeared at IEEE ICC'23 [1] and at IEEE ICASSP'24 [2].

This research has been funded in part by NSF under grant CNS-2129615.

channel estimation, link monitoring, and topology awareness:

- 1) Scheduling & signaling overhead: Mitigating the impact of unreliable wireless links requires scheduling of transmissions to manage interference, and the acquisition of channel state information (CSI, average or instantaneous) to compensate for signal fluctuations and link outages caused by fading. Executing tasks such as graph-coloring (used for scheduling in [18]–[20]), pilot assignment to minimize pilot contamination during channel estimation [21], monitoring large-scale propagation conditions, and reporting CSI feedback for power/rate adaptation may require inter-agent coordination and entail severe signaling overhead.
- 2) Topology information & weight design: The consensus step in {DGD} requires local topology awareness (set of neighbors in the mesh network), necessitating continuous monitoring of link qualities and path loss conditions. Furthermore, design of the mixing weights (see, e.g., [22], [23]) incurs additional signaling overhead.

The complexity of these tasks is exacerbated in mobile scenarios, such as swarms of UAVs, where the connectivity structure changes frequently. Therefore, achieving device-scalability of {DGD} in fully decentralized wireless systems, with a small signaling overhead footprint, remains an open challenge.

#### A. Novelty and Contributions

Addressing these challenges necessitates the design of decentralized optimization schemes tailored to wireless propagation environments. To meet these goals, in this paper we present a *Non-Coherent Over-the-Air* (NCOTA)-DGD algorithm. Unlike conventional DGD approaches that rely on orthogonal transmissions to mitigate interference (e.g., via TDMA), the core idea of NCOTA-DGD is to allow simultaneous transmissions, thus achieving device-scalability. To do so, NCOTA-DGD exploits the superposition property of wireless channels to estimate the consensus signal  $\mathbf{c}_i$ , in line with over-the-air computing (AirComp) paradigms proposed for FL [7], [24]–[28]. Nevertheless, AirComp typically relies on *coherent* alignment of signals at a common base station, achieved via channel inversion at the transmitters. In a decentralized setting, this condition cannot be met because signals are broadcast to multiple receivers, each receiving through a different channel.

To overcome this limitation, we develop a *non-coherent energy-based transmission technique* that operates without CSI, and we exploit a *noisy energy superposition property* of wireless channels at the receivers. Specifically, nodes encode their local state  $\mathbf{w}_i$  into transmitted energy levels and transmit simultaneously using a randomized scheme for half-duplex operation. Leveraging the circularly symmetric nature of wireless channels, the received signal energy is, on average, the sum of individual transmitted signal energies scaled by their respective channel gains, akin to the consensus signal  $\mathbf{c}_i$ , but with channel gains acting as mixing weights. Introducing a suitable consensus stepsize mitigates energy fluctuations in the received signal (errors in the consensus estimate). The benefits of NCOTA-DGD over conventional DGD schemes that rely on a mesh network [4], [17]–[20], [29]–[31] are two-fold:

- 1) Concurrent transmissions obviate the need for scheduling or inter-agent coordination, resulting in fast (albeit noisy) iter-

- ations. Consequently, device-scalability (when  $N$  is large) and scheduling-free operation are achieved.
- 2) By leveraging intrinsic channel properties for signal mixing, explicit design and knowledge of the mixing weights or topology information are not required. Furthermore, utilizing a non-coherent energy-based transmission and reception scheme obviates the need for CSI at transmitters or receivers. Consequently, the signaling overhead typically associated with these tasks is eliminated.

Yet, these benefits come at the cost of consensus estimation errors due to random energy fluctuations, requiring careful design of consensus and learning stepsizes to mitigate error propagation. Therefore, we develop a novel analysis of DGD with noisy consensus and noisy gradients, for the class of strongly-convex problems. We prove that, by choosing the learning stepsize as  $\eta_k \propto 1/k$  and the consensus stepsize as  $\gamma_k \propto k^{-3/4}$  at the  $k$ th iteration, the expected squared distance between the local and globally optimum models vanishes with rate  $\mathcal{O}(1/\sqrt{k})$ . This result improves prior works [18], [20], exhibiting non-vanishing errors, and [32] using fixed stepsizes.

Lastly, we propose extensions to cover a broad class of fading models and frequency-selective channels, including static channels as a special case. Numerical experiments on fashion-MNIST [33] image classification, formulated as regularized cross-entropy loss minimization, demonstrate faster convergence compared to state-of-the-art algorithms, including quantized DGD [32], a device-to-device wireless implementation of DGD [18], and AirComp-based FL [7]. Notably, our approach excels in densely deployed networks with large  $N$ , thus demonstrating its device-scalable design.

#### B. Related work

The study of distributed optimization algorithms to solve {P} is vast and can be traced back to the seminal work [34]. Several studies enable decentralized algorithms to function over finite capacity channels, using methods such as compression [35]–[37] or quantization [4], [14]–[17] of the transmitted signals. However, by assuming error-free communications, these works do not account for the impact of noise and fading in wireless channels. The impact of unreliable communications is investigated in [17], [29]–[31]. Yet, all these works inherently assume the use of orthogonal transmission strategies to mitigate interference (e.g., via TDMA scheduling), hence may not be device-scalable (when  $N$  is large), as observed earlier.

Recently, there has been significant interest in achieving device-scalability by leveraging the waveform superposition properties of wireless channels via AirComp [38], first studied from an information-theoretic perspective in [39]. However, most of these works are based on a centralized FL architecture with a base station acting as PS [7], [24]–[28], [40], hence they rely on assumptions unsuitable for decentralized settings:

- Coherent alignment: The works [7], [24]–[26] rely on channel inversion to achieve coherent alignment of the signals at a single receiver, the PS. Instead, in decentralized settings, multiple receivers receive signals through different channels. This diversity of channels makes simultaneous coherent alignment across multiple receivers impossible.
- Signaling overhead: Centralized FL schemes typically require meticulous power control and device scheduling to

enforce power constraints and ensure device participation, requiring CSI acquisition and monitoring of average path loss conditions [41]. However, the ensuing signaling overhead, often presumed error-free or its impact not assessed, might not scale effectively to decentralized networks.

- **Massive-MIMO:** The work [27] overcomes the need for CSI at the transmitters by assuming a large number of antennas at the PS and by leveraging the channel hardening effect. However, this assumption is not applicable to edge devices (e.g., UAVs) with compact form factor.
- **Noise-free downlink:** All these papers (except [26]) assume noise-free downlink. While reasonable for a PS with a typically larger power budget, this assumption may not hold under stringent power constraints of edge devices.

In contrast, NCOTA-DGD does not require CSI (at either transmitters or receivers) and does not rely on a large number of antennas, thanks to the use of non-coherent energy-based signaling strategies. It operates without power control or scheduling of devices, thus achieving device-scalable and scheduling-free operation. These features make NCOTA-DGD appealing to fully decentralized wireless systems.

Notable exceptions in the AirComp literature with star-based topology include [40], [42] (no *instantaneous* CSI) and [43] (partial CSI). In [40], local gradients are first encoded using random vector quantization [44], and then transmitted via preamble-based random access over flat-fading channels. However, this scheme is not suitable for fully decentralized systems: 1) The randomness introduced by random access increases the estimation variance at the receiver. 2) It relies on large antenna arrays at the PS to achieve vanishing optimality error, which may not be available, e.g., in small UAVs. 3) It hinges on average channel inversion to ensure unbiased gradient estimation at the PS. This is impractical in decentralized systems due to the signaling overhead associated with average CSI acquisition, and the diversity of channels across multiple receivers. 4) Non-negligible propagation delays and multipath create frequency-selectivity. To tackle 1-2), we design a *deterministic* energy-based encoding strategy and stepsizes to mitigate errors at the receivers, supported by a novel convergence analysis of DGD with noisy consensus. To tackle 3), we design a signal processing scheme tailored to unbiased consensus estimation, with weights given by average path loss conditions, without relying on their explicit knowledge. To tackle 4), we design mechanisms that enable operation over a broad class of frequency-selective channels, including static ones as a special case. In [42], blind over-the-air computation (BlairComp) of nomographic functions over multiple access channels is addressed using a Wirtinger flow method. However, [42] BlairComp does not ensure unbiased estimates, crucial for proving convergence of FL and DGD algorithms. The paper [43] uses channel phase correction at the transmitters to achieve coherent phase alignment at the PS. However, such alignment condition cannot be achieved towards multiple receivers, calling for a non-coherent energy superposition technique, NCOTA-DGD.

Recent works have developed algorithms for decentralized FL that are robust to wireless propagation impairments [18]–[20]. These schemes mitigate interference by decomposing the network into smaller non-interfering subgraphs, via graph-

coloring. In each subgraph, one device operates as the PS, enabling the use of AirComp techniques, coupled with a suitable consensus enforcing step similar to {DGD}. However, these schemes require topology awareness for graph-coloring, CSI feedback at the transmitters, power control, and scheduling of transmissions. Moreover, they rely on design of the mixing weights  $\omega$ , using methods such as [22], [23]. Coordinating the network to effectively execute these tasks may entail severe signaling overhead, and their complexity may not scale well to large networks. In contrast, in this paper, we leverage average path loss as a proxy for mixing weights, eliminating the need for their explicit knowledge and design, thus achieving device-scalability without CSI and inter-agent coordination.

Finally, the works [45]–[48] proposed *semi-decentralized* FL architectures, where edge devices collaborate with their neighbors unable to form a reliable direct link with the PS. However, these works inherit similar challenges outlined earlier under both centralized and decentralized architectures.

### C. Notation and Organization of the paper

For a set  $S \subset \mathbb{R}^d$ ,  $\text{int}(S)$  is its interior,  $\text{bd}(S)$  its boundary,  $\text{conv}(S)$  its convex hull. For matrix  $\mathbf{A}$ ,  $[\mathbf{A}]_{ij}$  is its  $ij$ th component,  $\mathbf{A}^\top$  its transpose,  $\mathbf{A}^H$  its complex conjugate transpose. Vectors are defined in column form. For (column) vector  $\mathbf{a}$ ,  $[\mathbf{a}]_i$  is its  $i$ th component,  $\|\mathbf{a}\| = \sqrt{\mathbf{a}^H \mathbf{a}}$  its Euclidean norm. For random vector  $\mathbf{a}$ , we let  $\|\mathbf{a}\|_{\mathbb{E}} \triangleq \sqrt{\mathbb{E}[\|\mathbf{a}\|^2]}$  ( $\|\mathbf{a}\|_{\mathbb{E}} = \|\mathbf{a}\|$  for deterministic  $\mathbf{a}$ ),  $\text{var}(\mathbf{a}) \triangleq \mathbb{E}[\|\mathbf{a}\|^2] - \|\mathbb{E}[\mathbf{a}]\|^2$  (variance) and  $\text{sdv}(\mathbf{a}) \triangleq \sqrt{\text{var}(\mathbf{a})}$  (standard deviation). We write  $\|\cdot\|_{\mathbb{E}|\mathcal{F}}$ ,  $\text{var}(\cdot|\mathcal{F})$  and  $\text{sdv}(\cdot|\mathcal{F})$  when the expectation is conditional on  $\mathcal{F}$ .  $\mathbf{a} \odot \mathbf{b}$  and  $\mathbf{a} \otimes \mathbf{b}$  are the Hadamard (entry-wise) and Kronecker products of  $\mathbf{a}$ ,  $\mathbf{b}$ . We define the following  $n$ -dimensional vectors/matrices (we omit  $n$  when clear from context): the  $m$ th standard basis vector  $\mathbf{e}_{n,m}$ , with  $m$ th component = 1, and 0 otherwise; the all ones and all zeros vectors  $\mathbf{1}_n$ ,  $\mathbf{0}_n$ ; the identity matrix  $\mathbf{I}_n$ .  $\mathbb{1}[A]$  is the indicator of event  $A$ .

The rest of this paper is organized as follows. In Secs. II-III, we present the system model and NCOTA-DGD. In Sec. IV, we delve into its convergence analysis, with proofs provided in the Appendix. In Sec. V, we present numerical results, followed by concluding remarks in Sec. VI. Supplementary details, including additional proofs and extended numerical evaluations, are provided in the supplemental document.

## II. SYSTEM MODEL AND NCOTA-DGD

Consider  $N$  wirelessly-connected nodes solving  $\{\mathbf{P}\}$  in a decentralized fashion. We divide time into frames of duration  $T$ . In this section, we consider a generic frame (iteration)  $k$ , and omit the dependence on  $k$ . In each iteration, we aim at emulating {DGD}, expressed in the equivalent form

$$\mathbf{w}_i \leftarrow \mathbf{w}_i + \gamma \mathbf{d}_i - \eta \nabla f_i(\mathbf{w}_i), \text{ with } \mathbf{d}_i = \sum_{j=1}^N \ell_{ij}(\mathbf{w}_i - \mathbf{w}_j), \quad (1)$$

where  $\mathbf{d}_i$  is the *disagreement signal*,  $\mathbf{w}_i + \gamma \mathbf{d}_i$  is equivalent to the consensus signal  $\mathbf{c}_i$  of {DGD},  $0 < \gamma \leq 1/\max_i \ell_{ii}$ , and  $\ell_{ij}$  are a set of Laplacian weights.<sup>1</sup> These are symmetric ( $\ell_{ij} = \ell_{ji} \leq 0$  for  $i \neq j$ ) and add to zero at each node ( $\ell_{ii} = -\sum_{j \neq i} \ell_{ij} > 0$ ). The flexibility in the choice of  $\ell$  will

<sup>1</sup>(1) maps to {DGD} with  $\omega_{ij} = -\gamma \ell_{ij}$  for  $i \neq j$ , and  $\omega_{ii} = 1 - \gamma \ell_{ii}$ .



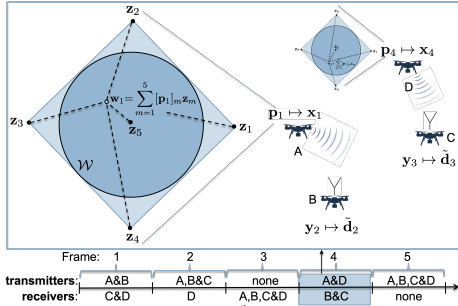


Fig. 1: Example of  $d=2$ -dimensional problem with  $N=4$  nodes. The circle represents the set  $\mathcal{W}$ , whereas the diamond represents the convex hull of  $M=5$  codewords from the CP0 codebook (Example 1),  $\mathbf{z}_1, \dots, \mathbf{z}_5$ . In frame  $k=4$ , nodes A and D encode their local state  $\mathbf{w}_i$  to a transmit signal  $\mathbf{x}_i$  (Eq. 5), and transmit simultaneously; receiving nodes C and D estimate the disagreement signal  $\hat{\mathbf{d}}_i$  from their received signal  $\mathbf{y}_i$  (Eqs. 7-12).

be exploited by designing a physical layer scheme that leverages the channel propagation conditions to mix the incoming signals – a departure from prior work that hinges on explicit design of  $\ell$ .

**Definition 1** (Laplacian matrix). We define the matrix  $\mathbf{L} \in \mathbb{R}^{N \times N}$  with components  $[\mathbf{L}]_{ij} = \ell_{ij}$ .  $\mathbf{L}$  is symmetric ( $\mathbf{L} = \mathbf{L}^\top$ ) and satisfies  $\mathbf{L} \cdot \mathbf{1} = \mathbf{0}$  (since  $\ell_{ii} = -\sum_{j \neq i} \ell_{ij}, \forall i$ ).

We assume that nodes operate under half-duplex constraints, i.e., they cannot simultaneously transmit and receive (Fig. 1). To accommodate this constraint, at the beginning of the frame, each node performs a random decision to either act as transmitter (denoted by the indicator variable  $\chi_i=1$  for node  $i$ ) or receiver ( $\chi_i=0$ ) in the current frame. These decisions are i.i.d. over iterations  $k$  and across nodes, and we let  $p_{\text{tx}} \triangleq \mathbb{P}(\chi_i = 1)$  be the transmission probability (designed in Lemma 2).

To achieve device-scalability, we allow the transmitting devices to transmit their local states  $\mathbf{w}_j$  simultaneously (vs orthogonal transmissions) and we leverage the superposition property of the wireless channel to estimate  $\hat{\mathbf{d}}_i$ . Unlike Air-Comp schemes developed for centralized FL that require coherent alignment of signals at the receiver, we employ *non-coherent energy estimation* methods, where information is conveyed as *signal energy*. As we will show, this method eliminates the need for instantaneous or average CSI at transmitters and receivers, but introduces errors in the estimation of  $\hat{\mathbf{d}}_i$ , calling for mitigation mechanisms developed in this work.

However, the local state  $\mathbf{w}_i$  includes sign information unsuitable for energy representation. To this end, transmitters employ an *energy-based encoding procedure* to map  $\mathbf{w}_i$  to an “energy” signal  $\mathbf{p}_i \geq \mathbf{0}$  (Sec. II-A). The latter controls energy levels across subcarriers of an OFDM symbol  $\mathbf{x}_i$ , then transmitted over the wireless channel (Sec. II-B). Receivers, on the other hand, receive the signal  $\mathbf{y}_i$  (Sec. II-C) and estimate the *disagreement signal* as  $\hat{\mathbf{d}}_i$  (Sec. II-D). Finally, all nodes update their local state  $\mathbf{w}_i$  by combining it with  $\hat{\mathbf{d}}_i$ , followed by local gradient descent (Sec. II-E). An example showcasing these steps is shown in Fig. 1.

#### A. Energy-based encoding: $\mathbf{w}_i$ mapped to “energy” signal $\mathbf{p}_i$

We assume that the optimizer of  $\{\mathbf{P}\}$  is known to lie within a closed, convex and bounded set  $\mathcal{W}$ . Thus,  $\mathbf{w}^* \in \mathcal{W}$ ,  $\mathbf{w}_i \in \mathcal{W}, \forall i$ , and  $\{\mathbf{P}\}$  is restricted within this set. For strongly-convex

global functions  $F(\cdot)$  with strong-convexity parameter  $\mu$  (see Assumption 2),  $\mathcal{W}$  may be chosen as the  $d$ -dimensional sphere with radius  $\frac{1}{\mu} \|\nabla F(\mathbf{0})\|$ ,<sup>2</sup> computed at initialization.

Since  $\mathcal{W}$  is bounded, it is contained by the convex-hull defined by a finite set of codewords, as depicted in Fig. 1. Concretely, let  $\mathcal{Z} = \{\mathbf{z}_m \in \mathbb{R}^d : m = 1, \dots, M\}$  be a codebook of  $M$  codewords such that  $\text{conv}(\mathcal{Z}) \supseteq \mathcal{W}$ .  $\mathcal{Z}$  is common knowledge among the nodes and remains fixed over iterates. Therefore, any  $\mathbf{w} \in \mathcal{W}$  may be represented as a convex combination of  $\mathcal{Z}$ . In other words, there exists a probability vector  $\mathbf{p} \in \mathbb{R}^M$  ( $\mathbf{1}^\top \cdot \mathbf{p} = 1, \mathbf{p} \geq \mathbf{0}$ ) such that

$$\mathbf{w} = \sum_{m=1}^M [\mathbf{p}]_m \mathbf{z}_m. \quad (2)$$

Given  $\mathbf{w}_i$  and the codebook  $\mathcal{Z}$ , node  $i$  then computes the associated probability vector  $\mathbf{p}_i$  satisfying the convex combination condition of (2). Unlike  $\mathbf{w}_i$  containing sign information, the non-negative vector  $\mathbf{p}_i$  is suitable to encode energy levels. An example of this construction is provided next and depicted in Fig. 1, based on the cross-polytope codebook [44].

**Example 1** (Cross-polytope- $\phi$  (CP $\phi$ ) codebook). Let  $\mathcal{W} \equiv \{\mathbf{w} : \|\mathbf{w}\| \leq r\}$  ( $d$ -dimensional sphere of radius  $r$ ). Consider  $M=2d+1$   $d$ -dimensional codewords defined as  $\mathbf{z}_{2d+1} = \mathbf{0}$ ,  $\mathbf{z}_m = \sqrt{dr} \mathbf{e}_m, \mathbf{z}_{d+m} = -\sqrt{dr} \mathbf{e}_m$ , for  $m = 1, \dots, d$ .

Then, for any  $\mathbf{w} \in \mathcal{W}$ , one can define the convex combination weights as  $[\mathbf{p}]_{2d+1} = 1 - \frac{1}{\sqrt{dr}} \|\mathbf{w}\|_1 - \phi$ , and, for  $m=1, \dots, d$ ,

$$[\mathbf{p}]_m = \frac{1}{\sqrt{dr}} ([\mathbf{w}]_m)^+ + \frac{\phi}{2d}, \quad [\mathbf{p}]_{d+m} = \frac{1}{\sqrt{dr}} (-[\mathbf{w}]_m)^+ + \frac{\phi}{2d},$$

where  $(\cdot)^+ = \max\{\cdot, 0\}$ ,  $\phi \in [0, 1 - \frac{1}{\sqrt{dr}} \|\mathbf{w}\|_1]$ , and  $\|\cdot\|_1$  is the  $\ell_1$  norm. With these value of  $\mathbf{z}$ ,  $\mathbf{p}$  and  $\phi$ , it can be verified by inspection that  $\mathbf{p}$  is a probability vector, i.e.  $[\mathbf{p}]_m \geq 0, \forall m$  and  $\sum_{m=1}^M [\mathbf{p}]_m = 1$  (this step requires using  $(x)^+ + (-x)^+ = |x|$ ), and that (2) holds (this step requires using  $(x)^+ - (-x)^+ = x$ ). We conclude that  $\mathbf{p}$  defines the desired convex combination. The cross-polytope vector quantization of [44] is a special case with  $\phi = 1 - \frac{1}{\sqrt{dr}} \|\mathbf{w}\|_1$  and  $[\mathbf{p}]_{2d+1} = 0$ .  $\square$

#### B. Transmission: $\mathbf{p}_i$ mapped to transmit signal $\mathbf{x}_i$

To provide insights into the energy-based transmission mechanism and the subsequent disagreement signal estimation at the receiver, it is convenient to rewrite  $\hat{\mathbf{d}}_i$  in (1) in the form<sup>3</sup>

$$\hat{\mathbf{d}}_i = \sum_{j \neq i} \ell_{ij} (\mathbf{w}_i - \mathbf{w}_j) = \sum_{m=1}^M \left( \sum_{j \neq i} -\ell_{ij} [\mathbf{p}_j]_m \right) (\mathbf{z}_m - \mathbf{w}_i), \quad (3)$$

where: in the first step, we restricted the sum to  $j \neq i$ , since  $\ell_{ii} (\mathbf{w}_i - \mathbf{w}_i) = 0$ ; in the second step, we replaced  $\mathbf{w}_j$  with its convex combination representation (2), and used the fact that  $\mathbf{p}_j$  is a probability vector, adding to one. This formulation suggests that, to estimate  $\hat{\mathbf{d}}_i$ , node  $i$  can first estimate

$$\sum_{j \neq i} -\ell_{ij} [\mathbf{p}_j]_m, \quad \forall m = 1, \dots, M, \quad (4)$$

since the terms  $\mathbf{z}_m - \mathbf{w}_i$  are known at node  $i$ . By interpreting  $[\mathbf{p}_j]_m \geq 0$  as the energy level transmitted by device  $j$  on the

<sup>2</sup>Strong convexity and the optimality condition  $\nabla F(\mathbf{w}^*) = \mathbf{0}$  imply  $\|\nabla F(\mathbf{0})\| = \|\nabla F(\mathbf{0}) - \nabla F(\mathbf{w}^*)\| \geq \mu \|\mathbf{0} - \mathbf{w}^*\|$ , hence  $\|\mathbf{w}^*\| \leq \|\nabla F(\mathbf{0})\| / \mu$ .

<sup>3</sup>Since  $\ell_{ij}$  are non-positive for  $i \neq j$ , for convenience we absorb the sign into  $-\ell_{ij}$ , so that  $-\ell_{ij} \geq 0$ .

$m$ th signal dimension, one can then interpret (4) as a *weighted sum* of these energies at the receiver side. Indeed, we will show that the wireless channel satisfies a *noisy energy superposition property* similar to (4), allowing direct estimation of (4) from received energies, with weights  $-\ell_{ij}$  corresponding to the average channel gains. To leverage this property, node  $i$  generates the transmit signal  $\mathbf{x}_i$  as described next.

We assume frequency-selective channels with non-negligible propagation delays between node pairs, hence the use of OFDM signaling. For clarity, each transmission is structured into one OFDM symbol with  $M$  subcarriers (matching the codebook size  $|\mathcal{Z}|$ ). We will extend this configuration to a generic number of subcarriers and/or OFDM symbols in Sec. III. Node  $i$  then maps  $\mathbf{p}_i$  to

$$[\mathbf{x}_i]_m = \sqrt{E \cdot M} \cdot [\mathbf{p}_i]_m, \quad \forall m = 1, \dots, M, \quad (5)$$

on the  $m$ th subcarrier, with energy per sample  $E$ . In other words,  $[\mathbf{p}_i]_m$  controls the energy allocated on the  $m$ th subcarrier (up to a scaling factor  $EM$ ). In (5), we opt for a deterministic map  $\mathbf{w}_i \mapsto \mathbf{p}_i \mapsto \mathbf{x}_i$ , in contrast to the random map of  $\mathbf{w}_i$  to  $\mathbf{z}_m$  according to the probability vector  $\mathbf{p}_i$ , used in [40], [44]. In fact, the random mapping introduces an additional source of randomness that increases the variance of the disagreement signal estimation.

**Remark 1.** The transmitted energy per sample satisfies

$$\frac{1}{M} \|\mathbf{x}_i\|^2 = \frac{1}{M} \sum_{m=1}^M |[\mathbf{x}_i]_m|^2 = E \sum_{m=1}^M [\mathbf{p}_i]_m = E,$$

since  $\mathbf{p}_i$  is a probability vector. Therefore, this scheme satisfies a target power constraint, enforced via the parameter  $E$ .  $\square$

### C. Received signal and Noisy energy superposition property

Focusing now on receiving nodes ( $\chi_i = 0$ ), let  $\mathbf{h}_{ij} \in \mathbb{C}^M$  be the frequency-domain channel vector between transmitter  $j$  and receiver  $i$ , so that  $[\mathbf{h}_{ij}]_m$  is the channel in the  $m$ th subcarrier. In this section, we assume Rayleigh fading channels (generalized to a broad class of channel models in Sec. III), independent across  $i, j$  and iterations  $k$ , so that  $[\mathbf{h}_{ij}]_m \sim \mathcal{CN}(0, \Lambda_{ij}), \forall m$  with average channel gain  $\Lambda_{ij}$  ( $=\Lambda_{ji}$  from channel reciprocity). Then, node  $i$  receives

$$[\mathbf{y}_i]_m = \sum_{j \neq i} \chi_j [\mathbf{h}_{ij}]_m [\mathbf{x}_j]_m + [\mathbf{n}_i]_m \quad (6)$$

on the  $m$ th subcarrier, where  $[\mathbf{n}_i]_m$  is AWGN noise with variance  $N_0$ . In vector form,

$$\mathbf{y}_i = \sum_{j \neq i} \chi_j \mathbf{h}_{ij} \odot \mathbf{x}_j + \mathbf{n}_i, \quad (7)$$

where  $\mathbf{n}_i \sim \mathcal{CN}(\mathbf{0}, N_0 \mathbf{I})$ . This signal model is the discrete-time equivalent baseband representation of the communication system, where  $\mathbf{x}$  is the signal before the inverse DFT and the cyclic prefix appending at the transmitter, and  $\mathbf{y}$  is the received signal after the DFT and cyclic prefix removal at the receiver. See, for instance, [49, Chapter 12.4]. In the next lemma, we demonstrate the energy superposition property, which will be directly tied to the estimation of (4).

**Lemma 1** (Energy superposition property). *The energy received on the  $m$ th subcarrier of node  $i$ ,  $|[\mathbf{y}_i]_m|^2$ , satisfies*

$$\mathbb{E}[|[\mathbf{y}_i]_m|^2] = EM \cdot p_{\text{tx}} \sum_{j \neq i} \Lambda_{ij} [\mathbf{p}_j]_m + N_0, \quad (8)$$

with  $\mathbb{E}$  computed with respect to the noise, Rayleigh fading, and random transmission decisions of nodes  $j \neq i$ .<sup>4</sup>

*Proof.* Let  $Y = \sum_j X_j$  be a sum of zero-mean ( $\mathbb{E}[X_j] = 0$ ) uncorrelated ( $\mathbb{E}[X_j X_{j'}^*] = 0$  for  $j \neq j'$ ) complex-valued random variables. Then, from the linearity of expectation,

$$\mathbb{E}[|Y|^2] = \mathbb{E}\left[\sum_j |X_j|^2 + \sum_{j, j' \neq j} X_j X_{j'}^*\right] = \sum_j \mathbb{E}[|X_j|^2]. \quad (9)$$

In (6),  $[\mathbf{y}_i]_m$  is a sum of uncorrelated random variables, since channels  $\mathbf{h}_{ij}$  and transmission decisions  $\chi_j$  are independent across  $j$ ,  $[\mathbf{n}_i]_m \sim \mathcal{CN}(0, N_0)$  is independent. Furthermore,  $\mathbb{E}[\chi_j [\mathbf{h}_{ij}]_m [\mathbf{x}_j]_m] = 0$  and  $\mathbb{E}[|\chi_j [\mathbf{h}_{ij}]_m [\mathbf{x}_j]_m|^2] = p_{\text{tx}} \Lambda_{ij} |[\mathbf{x}_j]_m|^2$ , since  $[\mathbf{h}_{ij}]_m \sim \mathcal{CN}(0, \Lambda_{ij})$  and  $\mathbb{P}(\chi_j = 1) = p_{\text{tx}}$ . Eq. (8) directly follows from (9) and (5).  $\square$

Lemma 1 states that, on average, the received energy is a superposition of transmitted energies, scaled by the average channel gains, plus the noise energy. It is thus apparent that  $|[\mathbf{y}_i]_m|^2$  contains information about (4), in the form of an unbiased estimate of it, with Laplacian weights corresponding to the average channel gains,  $-\ell_{ij} = \Lambda_{ij}, \forall i \neq j$ . This fact is exploited at the receiver to compute an unbiased estimate of the disagreement signal, discussed next.

### D. Disagreement signal estimation, $\tilde{\mathbf{d}}_i$

Lemma 1 suggests that node  $i$  can estimate  $\sum_{j \neq i} \Lambda_{ij} [\mathbf{p}_j]_m$  as

$$r_{im} = (1 - \chi_i) \frac{|[\mathbf{y}_i]_m|^2 - N_0}{p_{\text{tx}}(1 - p_{\text{tx}})EM}, \quad \forall m = 1, \dots, M. \quad (10)$$

Note that  $r_{im} = 0$  for transmitting nodes ( $\chi_i = 1$ ), consistent with the half-duplex constraint. To see that this is an unbiased estimate of  $\sum_{j \neq i} \Lambda_{ij} [\mathbf{p}_j]_m$ , we take the expectation of  $r_{im}$ , conditional on  $\chi_i$ , and use Lemma 1, yielding

$$\mathbb{E}[r_{im} | \chi_i] = \frac{1 - \chi_i}{1 - p_{\text{tx}}} \sum_{j \neq i} \Lambda_{ij} [\mathbf{p}_j]_m.$$

Finally, we take the expectation with respect to the transmit decision  $\chi_i \in \{0, 1\}$  and use  $\mathbb{E}[\chi_i] = p_{\text{tx}}$ , yielding

$$\mathbb{E}[r_{im}] = \sum_{j \neq i} \Lambda_{ij} [\mathbf{p}_j]_m, \quad \forall m = 1, \dots, M. \quad (11)$$

Therefore,  $r_{im}$  is an unbiased estimate of (4), with Laplacian weights given by the average channel gains,  $\ell_{ij} = -\Lambda_{ij}$  and  $\ell_{ii} = \sum_{j \neq i} \Lambda_{ij} > 0$ . It is then straightforward to generate an unbiased estimate of  $\mathbf{d}_i$ , by simply replacing  $\sum_{j \neq i} -\ell_{ij} [\mathbf{p}_j]_m$  in (3) with its unbiased estimate  $r_{im}$ , yielding

$$\tilde{\mathbf{d}}_i = \sum_{m=1}^M r_{im} (\mathbf{z}_m - \mathbf{w}_i). \quad (12)$$

<sup>4</sup>In this section, we implicitly assume that all expectations are conditional on  $\{\mathbf{w}_j, \forall j\}$ , hence on  $\{\mathbf{p}_j, \forall j\}$ .

Since  $\tilde{\mathbf{d}}_i$  is an unbiased estimate of  $\mathbf{d}_i$ , it follows that

$$\mathbb{E}[\tilde{\mathbf{d}}_i] = \sum_{m=1}^M \mathbb{E}[r_{im}](\mathbf{z}_m - \mathbf{w}_i) = \sum_{j \neq i} \Lambda_{ij}(\mathbf{w}_j - \mathbf{w}_i) = \mathbf{d}_i. \quad (13)$$

However, since this property holds only in expectation,  $\tilde{\mathbf{d}}_i$  exhibits zero-mean deviations around its expected value, due to noise, fading, random transmission decisions, and energy fluctuations in the wireless channel. The analysis of how these estimation errors impact convergence and are mitigated via a suitable stepsize design is conducted in Sec. IV.

The  $\ell$  values are indeed Laplacian weights, since they satisfy  $\ell_{ij} = -\Lambda_{ij} \leq 0$  for  $i \neq j$ ,  $\ell_{ij} = \ell_{ji}$  (average channel reciprocity,  $\Lambda_{ij} = \Lambda_{ji}$ ), and  $\ell_{ii} = \sum_{j \neq i} \Lambda_{ij} > 0$ . Accordingly, we define the Laplacian matrix  $\mathbf{L} \in \mathbb{R}^{N \times N}$  as in Definition 1, induced by the average channel gains  $\Lambda_{ij}$ .

### E. Local optimization state update

During the frame, node  $i$  computes an unbiased stochastic gradient  $\mathbf{g}_i$ , with  $\mathbb{E}[\mathbf{g}_i | \mathbf{w}_i] = \nabla f_i(\mathbf{w}_i)$ . It then updates  $\mathbf{w}_i$  as

$$\mathbf{w}_i \leftarrow \Pi[\mathbf{w}_i + \gamma \tilde{\mathbf{d}}_i - \eta \mathbf{g}_i], \quad (14)$$

where  $\Pi[\mathbf{a}]$  is a projection operator,

$$\Pi[\mathbf{a}] = \arg \min_{\mathbf{w} \in \mathcal{W}} \|\mathbf{w} - \mathbf{a}\|,$$

restricting the algorithm within the set  $\mathcal{W}$ , so that  $\mathbf{w}_i \in \mathcal{W}, \forall i$ .  $\gamma, \eta > 0$  are (possibly, time-varying) *consensus* and *learning* stepsizes, respectively: the former controls information diffusion and mitigates signal fluctuations in the disagreement signal estimation; the latter regulates the magnitude of gradient steps, hence the learning progress. As detailed in Sec. IV, their design is crucial to balancing these competing objectives.

These steps are repeated in frame  $k+1$  with the new local state  $\mathbf{w}_i$ , and so on. Note the key differences with respect to the conventional formulation (1): 1) the disagreement signal  $\mathbf{d}_i$  and gradient  $\nabla f_i(\mathbf{x}_i)$  are replaced with unbiased estimates,  $\tilde{\mathbf{d}}_i$  and  $\mathbf{g}_i$ , respectively; 2) the projection operator  $\Pi$ . Overall, NCOTA-DGD expressed in (14) can thus be interpreted as a projected DGD with noisy consensus and noisy gradients, whose convergence properties are studied in Sec. IV.

## III. GENERALIZATIONS

### A. More general frame structure

More generally, a frame is constituted of  $O$  OFDM symbols, each with  $SC$  subcarriers, defining  $Q = O \times SC \geq M$  resource units. An example is depicted in Fig. 2. Let  $q \in \{1, \dots, Q\} \equiv \mathcal{Q}$  be the  $q$ th resource unit, on a certain OFDM symbol and subcarrier. Unlike the previous section where  $Q = M$ , hence each signal dimension could only be mapped to a single subcarrier, we now have  $Q \geq M$ , which allows to map each component of the vector  $\mathbf{p}_i$  to multiple resources units. We thus define a partition of  $\mathcal{Q}$  into  $M$  non-empty sets,  $\mathcal{R}_1, \dots, \mathcal{R}_M$ , with  $\mathcal{R}_m \cap \mathcal{R}_{m'} \equiv \emptyset, \forall m \neq m'$  and  $\cup_{m=1}^M \mathcal{R}_m \equiv \mathcal{Q}$ . For instance, in Fig. 2,  $\mathcal{R}_1 \equiv \{1, 6, 11, 16, 21\}$ ,  $\mathcal{R}_2 \equiv \{2, 7, 12, 17, 22\}$ ,  $\mathcal{R}_3 \equiv \{3, 8, 13, 18, 23\}$ ,  $\mathcal{R}_4 \equiv \{4, 9, 14, 19, 24\}$ , containing 5 resource units, and  $\mathcal{R}_5 \equiv \{5, 10, 15, 20\}$  containing 4.

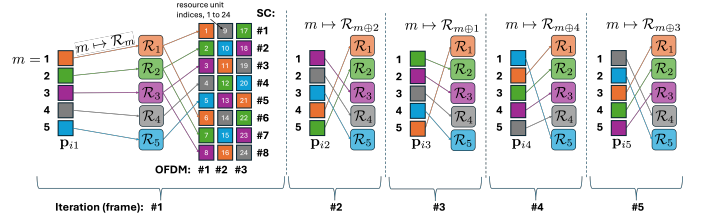


Fig. 2: Example of  $M=5$ -dimensional  $\mathbf{p}$  mapped to a frame containing  $O=3$  OFDM symbols, each with  $SC=8$  subcarriers, over 5 iterations. The color-coded sets  $\mathcal{R}_1, \dots, \mathcal{R}_5$  correspond to a partition of the  $Q=3 \times 8=24$  resource units (across subcarriers and OFDM symbols) allocated to a certain signal dimension. For instance, at iteration 1,  $m=1$  is allocated to  $\mathcal{R}_1$ , containing the resource units  $\{1, 6, 11, 16, 21\}$ . Frames #1 to #5 demonstrate the circular subcarrier shift (Sec. III-B). In this example, each signal dimension is mapped to all resource units across 5 iterations.

then map the  $m$ th component  $[\mathbf{p}_i]_m$  to the resource units  $\mathcal{R}_m$  by repetition. In vector notation, we define

$$\mathbf{u}_m \triangleq \sqrt{\frac{Q}{R_m}} \sum_{q \in \mathcal{R}_m} \mathbf{e}_q \in \mathbb{C}^Q, \quad (15)$$

with  $R_m \triangleq |\mathcal{R}_m|$ , as the vector describing the resource units that are activated in the set  $\mathcal{R}_m$ , with  $\|\mathbf{u}_m\| = \sqrt{Q}$ . In other words,  $\mathbf{u}_m$  has components equal to  $\sqrt{Q}/R_m$  in the indices in the set  $\mathcal{R}_m$ , and equal to zero otherwise. Note also that  $\{\mathbf{u}_m\}$  are orthogonal to each other,  $\mathbf{u}_m^H \mathbf{u}_{m'} = 0$  for  $m \neq m'$ , since  $\mathcal{R}_m \cap \mathcal{R}_{m'} \equiv \emptyset$ . With this definition, the allocation of  $[\mathbf{p}_i]_m$  to its associated resource units by repetition can be simply described as  $\sqrt{[\mathbf{p}_i]_m} \mathbf{u}_m$ , so that  $[\mathbf{p}_i]_m$  scales the energy allocated to  $\mathbf{u}_m$ , and the transmit signal is defined as

$$\mathbf{x}_i = \sqrt{E} \cdot \sum_{m=1}^M \sqrt{[\mathbf{p}_i]_m} \cdot \mathbf{u}_m.$$

With  $\mathbf{x}_i$  thus defined, the signal received by node  $i$  is given as in (7). Node  $i$  then computes the  $M$  energy signals

$$r_{im} = (1 - \chi_i) \sum_{q \in \mathcal{R}_m} \frac{|[\mathbf{y}_i]_q|^2 - N_0}{p_{\text{tx}}(1 - p_{\text{tx}})EQ}, \quad (16)$$

yielding (5)-(10) as a special case with  $Q=M$  and  $\mathcal{R}_m \equiv \{m\}$ . In (16), energies are aggregated across the resource units  $\mathcal{R}_m$  allocated on the  $m$ th component, rather than a single subcarrier in (10). To show that  $r_{im}$  is an unbiased estimate of (4), note that  $[\mathbf{x}_i]_q = \sqrt{EQ/R_m} \cdot \sqrt{[\mathbf{p}_i]_m}$  and

$$[\mathbf{y}_i]_q = \sum_{j \neq i} \chi_j [\mathbf{h}_{ij}]_q [\mathbf{x}_j]_q + [\mathbf{n}_i]_q, \quad \forall q \in \mathcal{R}_m.$$

Then, we use similar steps as in Lemma 1 to find

$$\mathbb{E}[|[\mathbf{y}_i]_q|^2] = \frac{EQ}{R_m} p_{\text{tx}} \sum_{j \neq i} \Lambda_{ij} [\mathbf{p}_j]_m + N_0, \quad \forall q \in \mathcal{R}_m, \quad (17)$$

so that  $\mathbb{E}[r_{im}] = \sum_{j \neq i} \Lambda_{ij} [\mathbf{p}_j]_m$  as in (11), after replacing (17) into the expectation of (16), and computing the expectation with respect to  $\chi_i$ . Therefore, (13) still holds.

### B. Broad class of channel models

The unbiasedness of  $\tilde{\mathbf{d}}_i$  in (13) is key to proving convergence in Sec. IV, but it may not hold under more general

channel models than those considered in Sec. II. For instance, if  $\mathbf{h}_{ij}$  remains fixed over iterations  $k$  (static channels),

$$\begin{aligned} \mathbb{E}[r_{im}] &= \sum_{j \neq i} \frac{1}{R_m} \sum_{q \in \mathcal{R}_m} |[\mathbf{h}_{ij}]_q|^2 [\mathbf{p}_j]_m \\ &+ 2p_{\text{tx}} \sum_{j, j' \neq i: j' < j} \frac{1}{R_m} \sum_{q \in \mathcal{R}_m} \text{re}([\mathbf{h}_{ij}]_q [\mathbf{h}_{ij'}]_q^*) \sqrt{[\mathbf{p}_j]_m [\mathbf{p}_{j'}]_m}, \end{aligned} \quad (18)$$

so that (11) no longer holds, violating the unbiasedness of the estimate  $\tilde{\mathbf{d}}_i$ . Compared to (11): 1) each component of  $\mathbf{p}_j$  experiences a different average channel gain,  $\frac{1}{R_m} \sum_{q \in \mathcal{R}_m} |[\mathbf{h}_{ij}]_q|^2$  for the  $m$ th component, instead of a common  $\Lambda_{ij}$ ; and 2) the cross-product terms  $\text{re}([\mathbf{h}_{ij}]_q [\mathbf{h}_{ij'}]_q^*)$  do not vanish. A bias term thus appears, that accumulates over time and leads to loss of the convergence properties. To recover the unbiasedness of  $\tilde{\mathbf{d}}_i$ , we introduce two mechanisms under a broad class of channels, including Rayleigh fading and static as special cases.

**Assumption 1.** The channels  $\mathbf{h}_{ij}$  are i.i.d. over iterations  $k$ .<sup>5</sup> We define the average gain across  $\mathcal{R}_m$  as

$$\Lambda_{ij}^{(m)} \triangleq \mathbb{E} \left[ \frac{1}{R_m} \sum_{q \in \mathcal{R}_m} |[\mathbf{h}_{ij}]_q|^2 \right],$$

and further across  $m$  as  $\Lambda_{ij} \triangleq \frac{1}{M} \sum_{m=1}^M \Lambda_{ij}^{(m)}$ .

*Random phase shift:* each transmitter applies a random phase shift to the transmit signal, uniform in  $[0, 2\pi]$ , i.i.d. over time and across nodes, and i.i.d. across resource units within the same set  $\mathcal{R}_m$ . Let  $[\theta_j]_q$  be the phase shift applied to the  $q$ th resource unit by node  $j$ . Then, the combined channel  $\tilde{\mathbf{h}}_{ij} = e^{j\theta_j} \odot \mathbf{h}_{ij}$  between transmitter  $j$  and receiver  $i$  ( $[\tilde{\mathbf{h}}_{ij}]_q = e^{j[\theta_j]_q} \cdot [\mathbf{h}_{ij}]_q$  on the  $q$ th resource unit) becomes circularly symmetric, yielding  $\mathbb{E}[\text{re}([\tilde{\mathbf{h}}_{ij}]_q [\tilde{\mathbf{h}}_{ij'}]_q^*)] = 0, \forall j \neq j'$ , upon taking the expectation on  $[\theta_j]_q$ . Therefore, the cross product terms in (18) vanish under a random phase shift.

*Coordinated circular subcarrier shift:* each transmitter applies a shift  $\varsigma$  to the mapping of signal components to resource units, i.e.,  $[\mathbf{p}_i]_m$  is mapped to the resource units in the set  $\mathcal{R}_{m \oplus \varsigma}$ ,<sup>6</sup>  $\varsigma$  is chosen uniformly at random in  $\mathcal{M} \equiv \{0, \dots, M-1\}$ , i.i.d. over time, and identical across devices (e.g., a pseudo-random sequence with a common seed). For instance, in Fig. 2,  $m$  is mapped to  $\mathcal{R}_m$  at iteration 1 ( $\varsigma=0$ ), to  $\mathcal{R}_{m \oplus 2}$  at iteration 2 ( $\varsigma=2$ ), to  $\mathcal{R}_{m \oplus 1}$  at iteration 3 ( $\varsigma=1$ ), to  $\mathcal{R}_{m \oplus 4}$  at iteration 4 ( $\varsigma=4$ ), and to  $\mathcal{R}_{m \oplus 3}$  at iteration 5 ( $\varsigma=3$ ). Thanks to this mechanism, each signal component goes through all resource units over multiple iterations, and experiences the same channel gain  $\Lambda_{ij}$ , on average.

Combining these two mechanisms, the transmit signal is

$$\mathbf{x}_i = \sqrt{E} \cdot e^{j\theta_i} \odot \sum_{m=1}^M \sqrt{[\mathbf{p}_i]_m} \cdot \mathbf{u}_{m \oplus \varsigma}. \quad (19)$$

Upon receiving  $\mathbf{y}_i$  as in (7), node  $i$  aggregates the energies received on  $\mathcal{R}_{m \oplus \varsigma}$  (the resource units allocated to  $m$ , accounting for the shift  $\varsigma$ ) to compute  $r_{im}$ , hence we modify (16) as

$$r_{im} = (1 - \chi_i) \sum_{q \in \mathcal{R}_{m \oplus \varsigma}} \frac{|[\mathbf{y}_i]_q|^2 - N_0}{p_{\text{tx}}(1 - p_{\text{tx}})EQ}. \quad (20)$$

<sup>5</sup>Static channels can be interpreted as a degenerate i.i.d. process in which  $\mathbf{h}_{ij}$  takes a deterministic value, with probability 1.

<sup>6</sup>Here,  $m \oplus \varsigma = 1 + \text{mod}(m-1+\varsigma, M)$  is the sum modulo  $M$ .

$\tilde{\mathbf{d}}_i$  is then computed as in (12), and the local model update follows (14). To show that  $r_{im}$  yields an unbiased estimate of (4), note that in the  $q$ th resource unit,  $q \in \mathcal{R}_{m \oplus \varsigma}$  we have

$$[\mathbf{y}_i]_q = \sum_{j \neq i} \chi_j [\mathbf{h}_{ij}]_q [\mathbf{x}_j]_q + [\mathbf{n}_i]_q, \quad \forall q \in \mathcal{R}_{m \oplus \varsigma},$$

with  $[\mathbf{x}_j]_q = e^{j[\theta_j]_q} \sqrt{EQ/R_{m \oplus \varsigma}} \sqrt{[\mathbf{p}_j]_m}$ . Then, we compute the expectation of  $|[\mathbf{y}_i]_q|^2$  with respect to the phase shifts, random transmissions of  $j \neq i$ , noise and channels, conditional on the subcarrier shift  $\varsigma$ . Thanks to the random phase shift  $[\theta_j]_q$ , i.i.d. across  $j$ ,  $\chi_j [\mathbf{h}_{ij}]_q [\mathbf{x}_j]_q$  are zero mean and uncorrelated across  $j$ . We can then use similar steps as in Lemma 1 to find

$$\mathbb{E}[|[\mathbf{y}_i]_q|^2 | \varsigma] = \frac{EQp_{\text{tx}}}{R_{m \oplus \varsigma}} \sum_{j \neq i} \mathbb{E}[|[\mathbf{h}_{ij}]_q|^2] [\mathbf{p}_j]_m + N_0, \quad \forall q \in \mathcal{R}_{m \oplus \varsigma}.$$

Using this expression in the expectation of (20), we then find

$$\begin{aligned} \mathbb{E}[r_{im} | \chi_i, \varsigma] &= \frac{1 - \chi_i}{1 - p_{\text{tx}}} \sum_{j \neq i} \frac{1}{R_{m \oplus \varsigma}} \sum_{q \in \mathcal{R}_{m \oplus \varsigma}} \mathbb{E}[|[\mathbf{h}_{ij}]_q|^2] [\mathbf{p}_j]_m \\ &= \frac{1 - \chi_i}{1 - p_{\text{tx}}} \sum_{j \neq i} \Lambda_{ij}^{(m \oplus \varsigma)} [\mathbf{p}_j]_m, \end{aligned}$$

with  $\Lambda_{ij}^{(m')}$  defined in Assumption 1. Therefore, the cross-product term in (18) vanishes, thanks to the circular symmetry of the equivalent channels  $\tilde{\mathbf{h}}_{ij} = e^{j\theta_j} \odot \mathbf{h}_{ij}$ . Finally, we compute the expectation with respect to  $\chi_i$  and  $\varsigma \sim \text{uniform}(\mathcal{M})$  (hence,  $m' = m \oplus \varsigma$  is uniform in  $\{1, 2, \dots, M\}$ ), yielding

$$\mathbb{E}[r_{im}] = \frac{1}{M} \sum_{m'=1}^M \sum_{j \neq i} \Lambda_{ij}^{(m')} [\mathbf{p}_j]_m = \sum_{j \neq i} \Lambda_{ij} [\mathbf{p}_j]_m,$$

with  $\Lambda_{ij}$  defined in Assumption 1. We conclude that  $r_{im}$  satisfies (11), so that  $\tilde{\mathbf{d}}_i$  is an unbiased estimate of  $\mathbf{d}_i$ , as in (13), and the convergence analysis of Sec. IV readily applies.

Therein, the convergence is dictated by the variance of the estimation error  $\tilde{\mathbf{d}}_i - \mathbb{E}[\tilde{\mathbf{d}}_i]$ , bounded in the next lemma. It shows the impact of: the variation of  $|[\mathbf{h}_{ij}]_q|^2$  around the average channel gain (averaged across resource units)  $\Lambda_{ij}$ , captured by the term  $\vartheta$ ; the variation of  $\hat{\lambda}_{ij}^{(m)}$  (sample average channel gain across  $\mathcal{R}_m$ ) around  $\Lambda_{ij}$ , captured by the term  $\varpi$ ; the maximum sum gain ( $\Lambda^*$ ). The lemma also provides a variance-minimizing design of the transmission probability  $p_{\text{tx}}$  (proof in the supplemental document).

**Lemma 2.** Consider channels satisfying Assumption 1. Assume that the resource units are evenly allocated among  $m = 1, \dots, M$ , i.e.,  $|R_m - Q/M| < 1, \forall m$  (e.g., Fig. 2). Let:

$$\vartheta \triangleq \max_{i, j \neq i} \frac{1}{\Lambda_{ij}} \left( \frac{1}{Q} \sum_{q=1}^Q \mathbb{E}[ (|[\mathbf{h}_{ij}]_q|^2 - \Lambda_{ij})^2 ] \right)^{1/2}, \quad (21)$$

$$\varpi \triangleq \max_{i, j \neq i} \frac{1}{\Lambda_{ij}} \left( \frac{1}{M} \sum_{m=1}^M \mathbb{E}[ (\hat{\lambda}_{ij}^{(m)} - \Lambda_{ij})^2 ] \right)^{1/2}, \quad (22)$$

$$\Lambda^* \triangleq \max_i \sum_{j \neq i} \Lambda_{ij}, \quad (23)$$

where  $\hat{\lambda}_{ij}^{(m)} = \frac{1}{R_m} \sum_{q \in \mathcal{R}_m} |[\mathbf{h}_{ij}]_q|^2$  is the sample average channel gain across the resource units in the set  $\mathcal{R}_m$ . Then,



---

**Algorithm 1** NCOTA-DGD iteration

- 1: **procedure** (at node  $i$ , given  $\mathbf{w}_i$ , circular shift  $\varsigma$ , stepsizes  $\eta, \gamma$ )
  - 2:   **Computation** (in parallel with communication): compute an unbiased stochastic gradient  $\mathbf{g}_i$  based on the local  $f_i$  at  $\mathbf{w}_i$ ;
  - 3:   **Random transmission decision** select  $\chi_i = 1$  with probability  $p_{\text{tx}}$ ,  $\chi_i = 0$  otherwise;
  - 4:   **Communication – if transmission** ( $\chi_i = 1$ ):
  - 5:     → Compute the convex combination  $\mathbf{p}_i$  (see Example 1);
  - 6:     → Generate random phase  $\theta_i$  and transmit signal  $\mathbf{x}_i$  via (19);
  - 7:     → Map  $\mathbf{x}_i$  to  $O$  OFDM symbols, each with SC subcarriers;
  - 8:     → Set  $\tilde{\mathbf{d}}_i = \mathbf{0}$ ;
  - 9:   **Communication – if reception** ( $\chi_i = 0$ ):
  - 10:    → Receive  $\mathbf{y}_i$  (see (7));
  - 11:    → Compute the  $M$  energy signals via (20);
  - 12:    → Estimate the disagreement signal  $\tilde{\mathbf{d}}_i$  via (12);
  - 13:    **DGD update:**  $\mathbf{w}_i \leftarrow \Pi[\mathbf{w}_i + \gamma\tilde{\mathbf{d}}_i - \eta\mathbf{g}_i]$  as in (14).
  - 14: **end procedure** repeat in the next iteration.
- 

$$\frac{1}{N} \sum_{i=1}^N \text{var}(\tilde{\mathbf{d}}_i) \leq \Sigma^{(1)} \triangleq \max_{\mathbf{z}, \mathbf{z}' \in \mathcal{Z}} \|\mathbf{z} - \mathbf{z}'\|^2$$

$$\times \frac{1}{1-p_{\text{tx}}} \left[ \frac{\sqrt{M}}{\sqrt{Q}} \sqrt{2(1+2\vartheta^2)} \Lambda^* + \frac{\sqrt{1+\varpi^2}}{\sqrt{p_{\text{tx}}}} \Lambda^* + \frac{\sqrt{M}}{\sqrt{Q}} \frac{N_0}{E p_{\text{tx}}} \right]^2.$$

The value of the transmission probability  $p_{\text{tx}}$  minimizing this bound is the unique solution in  $(0, 1)$  of

$$\sqrt{2(1+2\vartheta^2)} p_{\text{tx}}^{3/2} + \frac{\sqrt{Q}}{\sqrt{M}} \sqrt{1+\varpi^2} (2p_{\text{tx}} - 1) + \frac{N_0}{\Lambda^* E} \frac{3p_{\text{tx}} - 2}{\sqrt{p_{\text{tx}}}} = 0.$$

For Rayleigh fading channels discussed in Sec. II, and assuming the channel gains are independent across  $q \in \mathcal{R}_m$  (typically achieved by spacing apart the resource units belonging to the same  $\mathcal{R}_m$  by more than the channel's coherence bandwidth) we find  $\vartheta=1$  and  $\varpi \approx \sqrt{M/Q}$ . Algorithm 1 outlines the steps of NCOTA-DGD described in this section. Each OFDM symbol, with a communication bandwidth  $W_{\text{tot}}$ , has a duration  $T_{\text{ofdm}} = (\text{SC} + \text{CP})/W_{\text{tot}}$  (SC subcarriers; cyclic prefix length CP). With  $O$  OFDM symbols required to transmit the  $Q = O \cdot \text{SC}$ -dimensional signal  $\mathbf{x}_i$ , the frame duration is

$$T = O \cdot T_{\text{ofdm}} = W_{\text{tot}}^{-1} \cdot O \cdot (\text{SC} + \text{CP}), \quad (24)$$

irrespective of network size  $N$ . This highlights the device-scalability of NCOTA-DGD over large wireless networks, unlike a TDMA scheme where  $T$  grows linearly with  $N$ .

#### IV. CONVERGENCE ANALYSIS

In this section, we study the convergence of Algorithm 1 as it progresses over multiple iterations. Hence, we express the dependence of the signals and stepsizes on the iteration index  $k$ . Due to randomness of noise, fading, random transmissions, phase and circular subcarrier shifts at transmitters, Algorithm 1 induces a stochastic process. We denote by  $\mathcal{F}_k$  the  $\sigma$ -algebra generated by the signals up to frame  $k-1$ , including  $\mathbf{w}_{ik}$ ,  $\forall i$ . In essence, when taking expectations conditioned on  $\mathcal{F}_k$ , we consider the randomness generated during the  $k$ th iteration, conditional on the signals available at the start of that iteration.

To analyze NCOTA-DGD, we first stack its updates over the network, and make the error terms explicit (Sec. IV-A). We then introduce assumptions and definitions used in the analysis, commonly adopted in prior work (Sec. IV-B). We present the main convergence result in Sec. IV-C, then specialize it to constant (Sec. IV-D). and decreasing (Sec. IV-E) stepsizes.

#### A. Equivalent representation of NCOTA-DGD

We use lowercase variables for node-specific signals ( $\mathbf{a}_i$  for node  $i$ ) and uppercase variables for their concatenation over the network ( $Nd$ -dimensional vector  $\mathbf{A} = [\mathbf{a}_1^\top, \mathbf{a}_2^\top, \dots, \mathbf{a}_N^\top]^\top$ ). Thus,  $\mathbf{W}_k$ ,  $\mathbf{G}_k$ , and  $\tilde{\mathbf{D}}_k$  concatenate the  $\mathbf{w}_{ik}$ ,  $\mathbf{g}_{ik}$ , and  $\tilde{\mathbf{d}}_{ik}$  signals at iteration  $k$ . Additionally, we define  $\mathbf{W}^* = \mathbf{1}_N \otimes \mathbf{w}^*$  as the concatenation of  $\mathbf{w}^* = \arg \min_{\mathbf{w} \in \mathbb{R}^d} F(\mathbf{w})$ . Let

$$f(\mathbf{W}) = \sum_{i=1}^N f_i(\mathbf{w}_i). \quad (25)$$

Noting that  $\nabla f(\mathbf{W}) = [\nabla f_1(\mathbf{w}_1)^\top, \nabla f_2(\mathbf{w}_2)^\top, \dots, \nabla f_N(\mathbf{w}_N)^\top]^\top$ , we can then rewrite the update (14) as

$$\mathbf{W}_{k+1} = \Pi^N[\mathbf{W}_k + \gamma_k \tilde{\mathbf{D}}_k - \eta_k \mathbf{G}_k], \quad (26)$$

where  $\mathbb{E}[\mathbf{G}_k | \mathcal{F}_k] = \nabla f(\mathbf{W}_k)$  (unbiased gradient estimate) and  $\Pi^N[\cdot]$  is a projection onto  $\mathcal{W}^N$ . To facilitate the analysis, we define the errors  $\epsilon_k^{(1)}$  in the disagreement signal estimation, due to fading, noise, random transmissions, phase and circular subcarrier shifts, and  $\epsilon_k^{(2)}$  in the stochastic gradients. Namely,

$$\epsilon_k^{(1)} = \tilde{\mathbf{D}}_k - \mathbb{E}[\tilde{\mathbf{D}}_k | \mathcal{F}_k], \quad \epsilon_k^{(2)} = \mathbf{G}_k - \nabla f(\mathbf{W}_k).$$

By definition,  $\mathbb{E}[\epsilon_k^{(1)} | \mathcal{F}_k] = \mathbb{E}[\epsilon_k^{(2)} | \mathcal{F}_k] = \mathbf{0}$ . Letting  $\hat{\mathbf{L}} = \mathbf{L} \otimes \mathbf{I}_d$ , we then rewrite (26) in the equivalent form  $\mathbf{W}_{k+1}$

$$= \Pi^N \left[ \underbrace{(\mathbf{I} - \gamma_k \hat{\mathbf{L}}) \mathbf{W}_k - \eta_k \nabla f(\mathbf{W}_k)}_{(a)} + \underbrace{\gamma_k \epsilon_k^{(1)} - \eta_k \epsilon_k^{(2)}}_{(b)} \right], \quad (27)$$

where  $\mathbb{E}[\tilde{\mathbf{D}}_k | \mathcal{F}_k] = -\hat{\mathbf{L}} \mathbf{W}_k$  is obtained by concatenating  $\mathbb{E}[\tilde{\mathbf{d}}_{ik} | \mathcal{F}_k]$ , given by (13), and using the fact that

$$\mathbf{d}_i = \sum_{j=1}^N \ell_{ij} (\mathbf{w}_i - \mathbf{w}_j) = \sum_{j=1}^N \ell_{ij} \mathbf{w}_i - \sum_{j=1}^N \ell_{ij} \mathbf{w}_j = - \sum_{j=1}^N [\mathbf{L}]_{ij} \mathbf{w}_j$$

since  $\sum_{j=1}^N \ell_{ij} = 0$  for Laplacian weights. The term (a) in (27) specializes to the DGD update shown in (1) when  $\gamma_k = \gamma, \forall k$ ; the term (b) (referred to as "DGD noise" in the remainder), instead, captures the various sources of randomness. Following an approach similar to [12] for the analysis of DGD (therein, with fixed stepsize), we interpret the term (a) as a gradient descent, with stepsize  $\eta_k$ , based on the Lyapunov function

$$G_k(\mathbf{W}) \triangleq f(\mathbf{W}) + \frac{\gamma_k}{2\eta_k} \mathbf{W}^\top \cdot \hat{\mathbf{L}} \cdot \mathbf{W}.$$

Notably, the quadratic term in  $G_k$  enforces consensus in the network (in fact, it equals zero when  $\mathbf{w}_i = \mathbf{w}_j, \forall i, j$ ). Note that  $G_k$  is time-varying due to  $k$ -dependent stepsizes, thus generalizing [12], [32] that employ a fixed stepsize (hence a time-invariant  $G$ ). We can then express (27) compactly as

$$\mathbf{W}_{k+1} = \Pi^N[\mathbf{W}_k - \eta_k \nabla G_k(\mathbf{W}_k) + \gamma_k \epsilon_k^{(1)} - \eta_k \epsilon_k^{(2)}]. \quad (28)$$

#### B. Assumptions and Definitions

We study the convergence of (28) under standard assumptions, commonly adopted in prior work, e.g., [18], [20], [32].

**Assumption 2.** All  $f_i(\mathbf{w})$  are  $\mu$ -strongly convex,  $L$ -smooth.

A direct consequence is that the global  $F$  in  $\{\mathbf{P}\}$  and  $f$  in (25) are also  $\mu$ -strongly convex and  $L$ -smooth.



**Assumption 3.**  $\mathbf{w}^* \in \text{int}(\mathcal{W})$ , hence its distance from the boundary of  $\mathcal{W}$  satisfies  $\zeta \triangleq \min_{\mathbf{w} \in \text{bd}(\mathcal{W})} \|\mathbf{w} - \mathbf{w}^*\| > 0$ .<sup>7</sup>

$L$  is a Laplacian matrix (Definition 1), hence it is semidefinite positive with eigenvalues  $0 = \rho_1 \leq \dots \leq \rho_N$ . We assume that the average channel gains define a connected graph, so that the algebraic connectivity  $\rho_2$  is strictly positive [50].

**Assumption 4** (Algebraic connectivity of  $L$ ).  $\rho_2 > 0$ .

Finally, we make the following assumption on  $\epsilon_k^{(1)}$  and  $\epsilon_k^{(2)}$ .

**Assumption 5.** There exist  $\Sigma^{(1)}, \Sigma^{(2)} \geq 0$  such that

$$\frac{1}{N} \mathbb{E}[\|\epsilon_k^{(1)}\|^2 | \mathcal{F}_k] \leq \Sigma^{(1)}, \quad \frac{1}{N} \mathbb{E}[\|\epsilon_k^{(2)}\|^2 | \mathcal{F}_k] \leq \Sigma^{(2)}.$$

Closed-form expressions are given in Lemma 2 for  $\Sigma^{(1)}$ ,<sup>8</sup> and in Appendix A for  $\Sigma^{(2)}$ , under minibatch gradients.

Since  $\mathcal{W}$  is bounded, its diameter, defined below, is finite.

**Definition 2** (diameter of  $\mathcal{W}$ ).  $\text{dm}(\mathcal{W}) \triangleq \max_{\mathbf{w}, \mathbf{w}' \in \mathcal{W}} \|\mathbf{w} - \mathbf{w}'\|$ .

In Example 1,  $\text{dm}(\mathcal{W}) = 2r$ . Lastly, we define the gradient divergence at the global optimum  $\mathbf{w}^*$  (similar to [51]).

**Definition 3** (gradient divergence).  $\nabla^* \triangleq \max_i \|\nabla f_i(\mathbf{w}^*)\|$ .

### C. Main convergence result

The paper [32] considers *fixed* stepsizes and lacks a projection operator. The paper [4] considers a different class of functions (convex, non-smooth with bounded subgradients) and uses a projection, but its proof leverages the structure of the quantization error, under which  $\mathbf{W}_k + \gamma_k \tilde{\mathbf{D}}_k \in \mathcal{W}^N$ . This property does not hold in this paper, due to the potentially unbounded consensus error. Hence, their analyses cannot be readily extended to the setup of this paper, necessitating a new line of analysis, presented next.

We assume  $k \geq \bar{k}$  under a suitable iteration  $\bar{k} \geq 0$  (to be defined later). It represents a regime in which stepsizes become sufficiently small to satisfy the conditions stated in Theorem 3.<sup>9</sup> The main idea is to decompose the error between  $\mathbf{W}_k$  and the global optimum  $\mathbf{W}^*$  into: {1} the error between  $\mathbf{W}_k$  and the *noise-free dynamics*  $\tilde{\mathbf{W}}_k$  (obtained by setting the term (b) in (27) equal to 0), defined by the updates  $\tilde{\mathbf{W}}_{\bar{k}} = \mathbf{W}_{\bar{k}}$ ,

$$\tilde{\mathbf{W}}_{k+1} = \Pi^N[\tilde{\mathbf{W}}_k - \eta_k \nabla G_k(\tilde{\mathbf{W}}_k)], \quad \forall k \geq \bar{k}; \quad (29)$$

{2} the error between  $\tilde{\mathbf{W}}_k$  and the minimizer of the *time-varying* Lyapunov function  $G_k$ , defined at iteration  $k$  as

$$\mathbf{W}_k^* = \arg \min_{\mathbf{W} \in \mathcal{W}^N} G_k(\mathbf{W}); \quad (30)$$

and {3} the error between  $\mathbf{W}_k^*$  and  $\mathbf{W}^*$ . Accordingly,

$$\left( \mathbb{E} \left[ \sum \|\mathbf{w}_{ik} - \mathbf{w}^*\|^2 \right] \right)^{1/2} = \|\mathbf{W}_k - \mathbf{W}^*\|_{\mathbb{E}} \quad (31)$$

$$\begin{aligned} &= \|(\tilde{\mathbf{W}}_k - \tilde{\mathbf{W}}_k) + (\tilde{\mathbf{W}}_k - \mathbf{W}_k^*) + (\mathbf{W}_k^* - \mathbf{W}^*)\|_{\mathbb{E}} \\ &\leq \|\mathbf{W}_k - \tilde{\mathbf{W}}_k\|_{\mathbb{E}} + \|\tilde{\mathbf{W}}_k - \mathbf{W}_k^*\|_{\mathbb{E}} + \|\mathbf{W}_k^* - \mathbf{W}^*\|, \end{aligned} \quad (32)$$

<sup>7</sup>The analysis may be relaxed to the case when  $\mathbf{w}^*$  lies on the boundary of  $\mathcal{W}$  ( $\zeta = 0$ ), but it yields looser convergence results.

<sup>8</sup>Note that  $\frac{1}{N} \mathbb{E}[\|\epsilon_k^{(1)}\|^2 | \mathcal{F}_k] = \frac{1}{N} \sum_{i=1}^N \text{var}(\tilde{\mathbf{d}}_i | \mathcal{F}_k)$ .

<sup>9</sup>For  $k < \bar{k}$ , one can simply bound  $\|\mathbf{w}_{ik} - \mathbf{w}^*\| \leq \text{dm}(\mathcal{W})$ .

where the last step follows from Minkowski inequality [52, Lemma 14.10]. These terms are individually bounded in Theorem 3. A significant challenge in proving Theorem 3, in contrast to [32], stems from the time-varying behavior of  $G_k$ , caused by the use of time-varying stepsizes: in step {2}, one must carefully bound the *tracking error* associated with the changes in the  $G_k$ -minimizer  $\mathbf{W}_k^*$  over  $k$ . This issue is absent when using constant stepsizes as in [32].

**Theorem 3.** Assume  $\forall k \geq \bar{k}$ : **C1**:  $\eta_k(\mu + L) + \gamma_k \rho_N \leq 2$ ;

**C2**:  $\frac{\eta_k}{\gamma_k} \leq \frac{\zeta \cdot \mu \rho_2}{\sqrt{N} \nabla^* L}$ ; **C3**:  $\frac{\eta_k}{\eta_k} \leq \frac{\gamma_{k+1}}{\eta_{k+1}}$ . Then,

$$\frac{1}{\sqrt{N}} \|\mathbf{W}_k - \tilde{\mathbf{W}}_k\|_{\mathbb{E}} \leq \left[ \sum_{t=\bar{k}}^{k-1} P_{tk}^2 \left( \gamma_t^2 \Sigma^{(1)} + \eta_t^2 \Sigma^{(2)} \right) \right]^{\frac{1}{2}}, \quad (33)$$

$$\begin{aligned} \frac{1}{\sqrt{N}} \|\tilde{\mathbf{W}}_k - \mathbf{W}_k^*\|_{\mathbb{E}} &\leq \text{dm}(\mathcal{W}) \cdot P_{(\bar{k}-1)k} \\ &+ \frac{\nabla^* L}{\mu \rho_2} \sum_{t=\bar{k}}^{k-1} P_{tk} \left( 1 + \frac{L^2}{\mu \rho_2} \frac{\eta_t}{\gamma_t} \right) \left( \frac{\eta_t}{\gamma_t} - \frac{\eta_{t+1}}{\gamma_{t+1}} \right), \end{aligned} \quad (34)$$

$$\frac{1}{\sqrt{N}} \|\mathbf{W}_k^* - \mathbf{W}^*\|_{\mathbb{E}} \leq \frac{\nabla^* L}{\mu \rho_2} \frac{\eta_k}{\gamma_k}. \quad (35)$$

$$\text{where } P_{tk} \triangleq \prod_{j=t+1}^{k-1} (1 - \mu \eta_j), \quad \forall t \leq k-1. \quad (36)$$

*Proof.* See Appendix B.  $\square$

The term (33) captures the impact of the DGD noise through the variance terms  $\Sigma^{(1)}$  and  $\Sigma^{(2)}$ . Eq. (34) is composed of two terms: the first  $(\text{dm}(\mathcal{W}) P_{(\bar{k}-1)k})$  accounts for the initial error at time  $\bar{k}$ ; the second is a direct consequence of time-varying stepsizes (in fact, it is zero for constant ones); as highlighted previously, it represents the error accumulation due to tracking the changes of the  $G_k$ -minimizer  $\mathbf{W}_k^*$  over  $k$ . Eq. (35) shows that the minimizer  $\mathbf{W}_k^*$  of  $G_k$  approximates  $\mathbf{W}^*$  arbitrarily well when  $\eta_k/\gamma_k$  is small. We now specialize Theorem 3 to the case of constant stepsizes (Sec. IV-D), to gain insights on the design of decreasing stepsizes in Sec. IV-E.

### D. Constant stepsizes

Let  $\eta_k = \eta > 0$ ,  $\gamma_k = \gamma > 0$ ,  $\forall k$ . For the sake of exposition, further assume  $\Sigma^{(2)} = 0$ , and consider a target timeframe  $K$  when the algorithm stops. To satisfy **C1-C2** of Theorem 3, we need  $\eta(\mu + L) + \gamma \rho_N \leq 2$  and  $\frac{\eta}{\gamma} \leq \frac{\zeta \cdot \mu \rho_2}{\sqrt{N} \nabla^* L}$  with  $\bar{k} = 0$ . Then, at algorithm termination (33)-(35) specialize as

$$\frac{1}{\sqrt{N}} \|\mathbf{W}_K - \tilde{\mathbf{W}}_K\|_{\mathbb{E}} \leq \sqrt{\Sigma^{(1)}} \frac{\gamma}{\sqrt{\eta \mu}}, \quad (37)$$

$$\frac{1}{\sqrt{N}} \|\tilde{\mathbf{W}}_K - \mathbf{W}_K^*\|_{\mathbb{E}} \leq \text{dm}(\mathcal{W}) (1 - \mu \eta)^k \leq \text{dm}(\mathcal{W}) e^{-\mu \eta K}, \quad (38)$$

$$\frac{1}{\sqrt{N}} \|\mathbf{W}_K^* - \mathbf{W}^*\|_{\mathbb{E}} \leq \frac{\nabla^* L}{\mu \rho_2} \frac{\eta}{\gamma}. \quad (39)$$

To make these errors small,  $\gamma/\sqrt{\eta}$ ,  $\eta/\gamma$  and  $e^{-\mu \eta K}$  need all be small, yielding a trade-off between  $\gamma$  and  $\eta$ . To make  $e^{-\mu \eta K} \rightarrow 0$  as  $K \rightarrow \infty$  we require  $\eta \alpha K^{-(1-\epsilon)}$  for small  $\epsilon > 0$ . With such choice of  $\eta$ , the trade-off between (37) and (39) is optimized by making  $\gamma/\sqrt{\eta} \propto \eta/\gamma$ , yielding  $\gamma \propto K^{-3/4(1-\epsilon)}$ . Under this choice, the three error terms (37)-(39), hence the overall error (31), become of order  $\mathcal{O}(K^{-1/4(1-\epsilon)})$  for target  $K$  iterations. A similar convergence rate is shown in [32]

under a different setup:<sup>10</sup> it assumes quantization, error-free communications, constant stepsizes and no projection. This analysis unveils some drawbacks of using constant stepsizes: 1) faster convergence is achieved with smaller  $\epsilon$  (approaching  $\mathcal{O}(K^{-1/4})$ ), at the cost of larger (38); 2) tuning of  $\eta$  and  $\gamma$  requires prior knowledge of the target timeframe  $K$ , as well as of  $\rho_2, \rho_N, \zeta, \nabla^*$  to satisfy **C1-C2** of Theorem 3; 3) the stepsize conditions needed to ensure these convergence properties may be overly stringent to meet in practical scenarios. These limitations are overcome via decreasing stepsizes.

### E. Decreasing stepsizes

The constant stepsize analysis suggests that  $\gamma_k \propto k^{-3/4}$  and  $\eta_k \propto k^{-1}$ . Accordingly, we choose  $\gamma_k = \gamma_0(1 + \delta k)^{-3/4}$  and  $\eta_k = \eta_0(1 + \delta k)^{-1}$  with initial stepsizes  $\gamma_0, \eta_0$ . The parameter  $\delta > 0$ , termed *decay rate*, controls how quickly  $\eta_k, \gamma_k$  decrease over time. With this choice: 1)  $\gamma_k/\eta_k$  is non-decreasing in  $k$  (**C3** of Theorem 3); 2) since  $\eta_k, \gamma_k, \eta_k/\gamma_k \rightarrow 0$  for  $k \rightarrow \infty$ , there exists  $\bar{k} \geq 0$  satisfying **C1-C2** of Theorem 3  $\forall k \geq \bar{k}$ . The following result specializes Theorem 3 to this choice.

**Theorem 4.** Let  $\gamma_k = \gamma_0(1 + \delta k)^{-3/4}$ ,  $\eta_k = \eta_0(1 + \delta k)^{-1}$  with  $\delta \leq \frac{4}{5}\mu\eta_0$ . Then,  $\forall k \geq \bar{k}$ ,

$$\frac{1}{\sqrt{N}} \|\mathbf{W}_k - \tilde{\mathbf{W}}_k\|_{\mathbb{E}} \leq \frac{\sqrt{5}e}{2\sqrt{\mu}} \left[ \frac{\gamma_0}{\sqrt{\eta_0}} \sqrt{\Sigma^{(1)}} + \sqrt{\eta_0 \Sigma^{(2)}} (1 + \delta k)^{-1/4} \right] (1 + \delta k)^{-1/4}, \quad (40)$$

$$\frac{1}{\sqrt{N}} \|\tilde{\mathbf{W}}_k - \mathbf{W}_k^*\|_{\mathbb{E}} \leq \text{dm}(\mathcal{W}) \left( 1 + \frac{\delta(k - \bar{k})}{1 + \delta\bar{k}} \right)^{-5/4} + \frac{\nabla^* L e \eta_0}{\mu \rho_2} \frac{1}{4\gamma_0} \left( 1 + \frac{L^2 \eta_0}{\mu \rho_2 \gamma_0} (1 + \delta k)^{-1/4} \right) (1 + \delta k)^{-1/4}, \quad (41)$$

$$\frac{1}{\sqrt{N}} \|\mathbf{W}_k^* - \mathbf{W}^*\| \leq \frac{\nabla^* L \eta_0}{\mu \rho_2 \gamma_0} (1 + \delta k)^{-1/4}. \quad (42)$$

*Proof.* See Appendix C.  $\square$

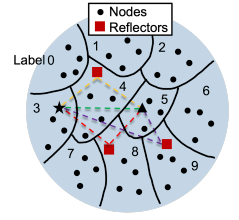
Notably, this result holds for any initial stepsizes  $\eta_0, \gamma_0 > 0$ , unlike the constant stepsize case which demands strict adherence to conditions **C1-C2**. This flexibility allows for numerical optimization of  $\eta_0$  and  $\gamma_0$  while maintaining the convergence guarantees of Theorem 4, highlighting a trade-off in their choice. Tuning  $\gamma_0$  reflects a delicate balance between facilitating information propagation (favored by larger  $\gamma_0$ ) and mitigating error propagation (smaller  $\gamma_0$ ). As to the choice of  $\delta$ , as it increases, both  $\eta_k$  and  $\gamma_k$  get smaller, reducing  $\bar{k}$ —the iteration index meeting the convergence conditions of Theorem 3. Thus, the regime  $k \geq \bar{k}$  is attained more rapidly. At the same time, terms like  $(1 + \delta k)^{-1/4}$  and  $(1 + \delta(k - \bar{k})) / (1 + \delta\bar{k})^{-5/4}$  get smaller. We conclude that  $\delta = \frac{4}{5}\mu\eta_0$  minimizes (40)-(42), further motivating the use of decreasing vs constant ( $\delta \rightarrow 0$ ) stepsizes. This design insight is corroborated numerically in Fig. 6 of the supplemental document.

Combining these results into (32), it readily follows that

$$\mathbb{E} \left[ \frac{1}{N} \sum_i \|\mathbf{w}_{ik} - \mathbf{w}^*\|^2 \right] = \mathcal{O}(1/\sqrt{k}). \quad (43)$$

<sup>10</sup>Note that  $\alpha, \epsilon, \delta, T$  used in [32, Theorem 1] map as  $\alpha \mapsto \eta/\gamma, \epsilon \mapsto \gamma, \delta \mapsto (1 - \epsilon)/2, T \mapsto K$  in our paper

Fig. 3: Example of *spatially-dependent* deployment scenario with  $N = 40$  nodes. Each node holds data from only one class, indicated by the label indices '0' to '9' (4 nodes per class). For instance, node  $\star$  holds data from class '3'. With 3 reflectors, there are 4 signal paths, shown in the figure between a generic transmitter ( $\star$ ) and receiver ( $\blacktriangle$ ) pair.



To get some intuition behind this result, consider (27) with fixed consensus stepsize and no projection:

$$\mathbf{W}_{k+1} = (\mathbf{I} - \gamma \hat{\mathbf{L}}) \mathbf{W}_k - \eta_k \nabla f(\mathbf{W}_k) + \epsilon_k^{(tot)}, \quad (44)$$

where  $\epsilon_k^{(tot)} \triangleq \gamma \epsilon_k^{(1)} - \eta_k \epsilon_k^{(2)}$  is the overall DGD noise. These updates resemble the DGD algorithm (1), where  $\mathbb{E}[\|\mathbf{W}_k^* - \mathbf{W}^*\|^2] = \mathcal{O}(1/k)$  with stepsize  $\eta_k \propto 1/k$ , provided that  $\text{var}(\epsilon_k^{(tot)}) \propto k^{-2}$ . This condition holds when stochastic gradients are the sole source of DGD noise, since  $\|-\eta_k \epsilon_k^{(2)}\|_{\mathbb{E}}^2 \propto \eta_k^2 \propto k^{-2}$ , but it fails in the presence of consensus error, which becomes dominant. To mitigate this error, a decreasing consensus stepsize  $\gamma_k \propto k^{-3/4}$  is required, at the expense of slower convergence ( $\mathcal{O}(1/\sqrt{k})$ ).

## V. NUMERICAL RESULTS

We solve a classification task on fashion-MNIST [33], a dataset of grayscale images of fashion items from 10 classes.

**Network deployment:**  $N$  nodes (200, unless otherwise stated) are spread uniformly at random over a circular area of 2km radius. They communicate over a  $W_{\text{tot}} = 5\text{MHz}$  bandwidth,  $f_c = 3\text{GHz}$  carrier frequency, with  $P_{tx} = 20\text{dBm}$  power ( $E = P_{tx}/W_{\text{tot}}$ ). The noise power spectral density at the receivers is  $N_0 = -173\text{dBmW/Hz}$ . We use OFDM signaling with  $SC = 512$  subcarriers and a cyclic prefix of length  $CP = 133$ , accommodating propagation delays up to  $26.6\mu\text{s}$ . Each OFDM symbol has duration  $T_{\text{ofdm}} = (SC + CP)/W_{\text{tot}} = 129\mu\text{s}$ .

**Channel model:** We generate spatially consistent channels by randomly placing 3 reflectors (see Fig. 3). The channel between transmitter  $j$  and receiver  $i$  in the  $m$ th subcarrier is

$$[\mathbf{h}_{ij}]_m = \sum_{p=0}^3 \sqrt{\alpha_{ijp}} \phi_{ijp} e^{-j2\pi\tau_{ijp} W_{\text{tot}} m / SC},$$

where  $p=0$  is the LOS path and  $p \neq 0$  are the reflected paths;  $\tau_{ijp} = \frac{d_{ijp}}{c}$  is the path propagation delay,  $d_{ijp}$  is its distance traveled,  $c$  is the speed of light;  $\alpha_{ijp} = \left(\frac{c}{4\pi f_c d_{ijp}}\right)^2$  is the path gain, based on Friis' free space equation;  $\phi_{ijp}$  is the fading coefficient:  $|\phi_{ijp}| = 1$  with uniform phase for the LOS path,  $\phi_{ijp} \sim \mathcal{CN}(0, 1)$  (Rayleigh fading) for reflected paths.

**Data deployment:** The global dataset is constituted of 1000 low-resolution images (100 from each class), distributed across the  $N$  nodes. To emulate data heterogeneity, each node has a local dataset with  $1000/N$  images from a single class,  $c_i \in \{0, \dots, 9\}$  for node  $i$ , so that  $N/10$  nodes have label (fashion item) '0',  $N/10$  have label '1', and so on. Cooperation is then necessary to solve the classification task, due to lack of examples of other classes at any single node. Each  $7 \times 7$  pixels image is converted into a 50-dimensional feature  $\mathbf{f} \in \mathbb{R}^{50}$  (including a fixed offset) and normalized to  $\|\mathbf{f}\|_2 = 1$ .

Furthermore, we consider two different spatial data distributions. In the *spatially-i.i.d.* case, the nodes' labels are assigned in an i.i.d. fashion to each node, irrespective of their location. In the *spatially-dependent* case, shown in Fig. 3, the circular

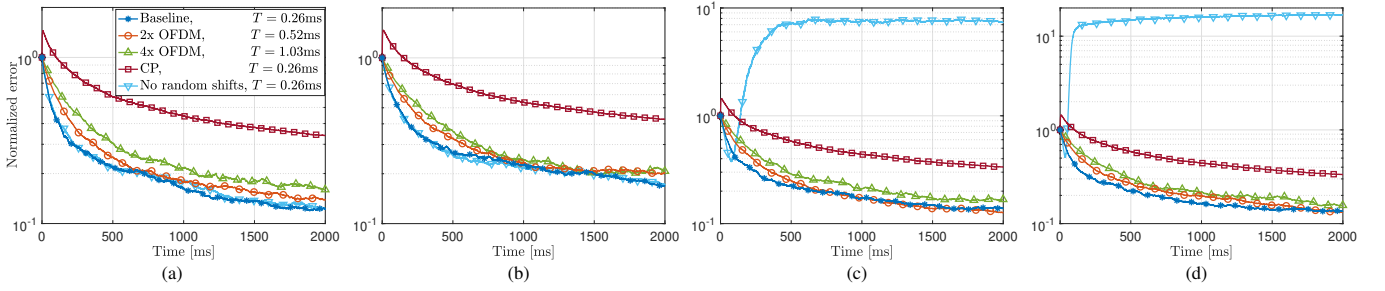


Fig. 4: Normalized error vs time, for different configurations of NCOTA-DGD and four different scenarios. The common legend is shown in the left figure, and shows the frame duration of each configuration. (a) Spatially-i.i.d. labels and i.i.d. channels; (b) Spatially-dependent labels and i.i.d. channels; (c) Spatially-i.i.d. labels and block-fading channels (2ms coherence time); (d) Spatially-i.i.d. labels and static channels.

region is divided into 10 subregions, each containing an equal number of nodes with the same label, so that the label of a certain node depends on its position in the network.

**Optimization problem:** We solve the task via regularized cross-entropy loss minimization, with loss function

$$\phi(c, \mathbf{f}; \mathbf{w}) = \frac{\mu}{2} \|\mathbf{w}\|_2^2 - \ln \left( \frac{\exp\{\mathbf{f}^\top \mathbf{w}^{(c)}\}}{\sum_{j=0}^9 \exp\{\mathbf{f}^\top \mathbf{w}^{(j)}\}} \right)$$

for feature  $\mathbf{f}$  with label  $c$ , where:  $\mathbf{w}^\top = [\mathbf{w}^{(1)\top}, \dots, \mathbf{w}^{(9)\top}] \in \mathbb{R}^d$  is a  $d=450$ -dimensional parameter vector, with  $\mathbf{w}^{(c)} \in \mathbb{R}^{50}$ ,  $\mathbf{w}^{(0)} = \mathbf{0}$ ,  $\mu = 0.001 > 0$ . Hence,  $f_i(\mathbf{w}) = \frac{1}{|\mathcal{D}_i|} \sum_{\mathbf{f} \in \mathcal{D}_i} \phi(c_i, \mathbf{f}; \mathbf{w})$ . All  $f_i(\mathbf{w})$  and the global function  $F(\mathbf{w})$  are  $\mu$ -strongly-convex and  $L = \mu + 2$ -smooth.  $\mathcal{W}$  is the  $d$ -dimensional sphere centered at  $\mathbf{0}$  with radius  $r = \frac{1}{\mu} \|\nabla F(\mathbf{0})\|$  (Example 1).

**Computational model:** Each gradient computation  $\nabla \phi(\cdot)$  on a single datapoint takes  $T_{\text{gr}} = 30\mu\text{s}$ .<sup>11</sup> Hence, computing the gradient over a minibatch  $\mathcal{B}_i \subseteq \mathcal{D}_i$  takes  $|\mathcal{B}_i| T_{\text{gr}}$ . Since gradient computations are done in parallel with communications, we set the minibatch size as  $|\mathcal{B}_i| = \min\{\lceil T/T_{\text{gr}} \rceil, |\mathcal{D}_i|\}$ , consistent with the frame duration  $T$  specific to each algorithm.

#### A. Comparison of variants of NCOTA-DGD

We compare different configurations of NCOTA-DGD:

- **Baseline** uses the CP0 codebook of Example 1 with  $M = 2d + 1 = 901$  codewords, requiring two OFDM symbols ( $Q = 1024$ ), and yielding a frame of duration  $T = 2T_{\text{ofdm}} = 258\mu\text{s}$ . It follows Algorithm 1 with parameters  $\eta_0 = \frac{2}{\mu + L}$ ,  $\gamma_0 = \frac{0.05}{\rho_2}$  and  $\delta = \frac{4}{5}\mu\eta_0$ , in line with Theorem 4 and as motivated in the discussion following Theorem 4. The transmission probability  $p_{\text{tx}}$  is set as in Lemma 2, with  $\vartheta = 1$  and  $\varpi \approx \sqrt{M/Q}$ . This choice of parameters is corroborated by numerical evaluations in the supplemental document (Fig. 6).
- **2xOFDM** and **4xOFDM** are the same as **Baseline**, but they use  $\times 2$  and  $\times 4$  as many OFDM symbols, yielding  $Q = 2048$  ( $T = 516\mu\text{s}$ ) and  $Q = 4096$  ( $T = 1032\mu\text{s}$ ), respectively. From Lemma 2, larger  $Q$  yields smaller noise in the consensus estimation, at the cost of longer frame duration  $T$ .
- **CP** is the same as **Baseline**, but it employs the conventional cross-polytope codebook of [44] with  $\phi = 1 - \frac{1}{\sqrt{dr}} \|\mathbf{w}_i\|_1$ .
- **No random shifts** is the same as **Baseline**, but it does not apply the random phase and coordinated circular subcarrier shifts on the transmitted signal, described in Sec. III-B.

All variants are initialized as  $\mathbf{w}_i = \mathbf{0}, \forall i$ . We evaluate them on four different scenarios as described in the caption of Fig. 4, differing in the data deployments (spatially-i.i.d. or -dependent) and channel fading properties: i.i.d., in which

channels are i.i.d. over frames; block-fading, in which they vary every 2ms (coherence time); and static, in which they remain fixed over the entire simulated interval.

In Fig. 4, we plot the *normalized error*,  $\frac{\mathbb{E}[\sum_i \|\mathbf{w}_i - \mathbf{w}^*\|^2]}{N \|\mathbf{w}^*\|^2}$ , versus the execution time ( $kT$  after  $k$  iterations). Here,  $\mathbb{E}$  denotes a sample average across 20 algorithm trajectories generated through independent realizations of network deployment, channels, AWGN noise, and randomness used by the algorithm (transmission decisions, phase and circular subcarrier shifts, minibatch gradient selections). We notice that **Baseline** consistently performs the best across all different scenarios. It has shorter frame duration but higher variance of the disagreement signal estimation (Lemma 2) than **2xOFDM** and **4xOFDM**. This demonstrates that it is preferable to perform more frequent, albeit noisier, iterations of DGD. The CP0 codebook of **Baseline** has lower variance of the disagreement signal estimation than **CP**, yielding better performance.<sup>12</sup> **No random shifts** diverges with non-i.i.d. channels (Figs. 4.c-d), due to a bias term in the disagreement signal estimation (see (18)), which accumulates over time. In contrast, all other schemes employing the random phase and circular subcarrier shifts developed in Sec. III-B are not affected by different channel fading properties. Fig. 4.b depicts a slight degradation in performance for all schemes in the spatially-dependent label scenario. To explain this behavior, consider the receiving node labeled as  $\blacktriangle$  in Fig. 3, carrying label '5': it receives strong signals from the nearby nodes carrying the same label '5' (less informative to  $\blacktriangle$ ), but weaker signals from the nodes with label '0' (more informative to  $\blacktriangle$ ). This results in slower propagation of information across the network.

#### B. Comparison with state-of-the-art (SoA) schemes

In the remainder, we use the **Baseline** configuration of NCOTA-DGD, described in Sec. V-A, due to its superior performance observed in Fig. 4. We compare it with adaptations of SoA works to the setting of this paper:

- **QDGD-LPQ/-VQ**, adaptation of [32], which investigates the design and convergence analysis of Quantized-DGD under fixed learning and consensus stepsizes. Yet, it assumes error-free communications, hence is not tailored to wireless systems affected by fading and interference. To adapt [32] to our setting, nodes transmit over orthogonal channels via OFDMA, i.e., multiple nodes may transmit simultaneously on the same OFDM symbol, across orthogonal subcarriers.

<sup>12</sup>Analysis of this behavior is left for future work; it requires a tighter bound than Lemma 2 (valid under any codebook), by exploiting properties of CP $\phi$ .

<sup>11</sup>Estimated based on a 2.4 GHz 8-Core Intel Core i9 processor.



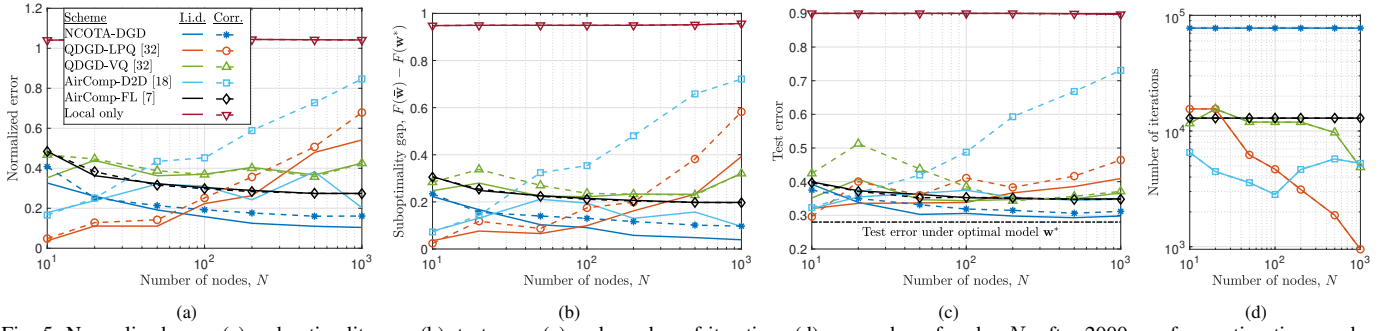


Fig. 5: Normalized error (a), suboptimality gap (b), test error (c) and number of iterations (d) vs number of nodes  $N$ , after 2000ms of execution time, under spatially-i.i.d. (solid lines) and -dependent (dashed lines with markers) label scenarios, with i.i.d. channels over frames. Common legend shown in figure (a).

Node  $i$  quantizes  $\mathbf{w}_i$  using  $B$  bits, and broadcasts the payload over the wireless channel on the assigned subcarriers  $\mathcal{S}_i$ . Upon receiving the signal broadcast by node  $j$ , node  $i$  decodes the payload correctly (denoted by the success indicator  $\chi_{ij}=1$ ) if and only if  $B < \sum_{s \in \mathcal{S}_j} \log_2(1 + \frac{E}{N_0} \frac{SC}{|\mathcal{S}_j|} |[\mathbf{h}_{ij}]_s|^2)$ , where  $\mathcal{S}_j$  are the resource units allocated to node  $j$ . Otherwise, an outage occurs ( $\chi_{ij}=0$ ). Let  $N_{rx,i}$  be the number of packets successfully received, and  $\hat{\mathbf{w}}_j$  the reconstruction of  $\mathbf{w}_j$  induced by the quantization operator. Node  $i$  then follows the updates (14), with  $\tilde{\mathbf{d}}_i = \frac{1}{N_{rx,i}} \sum_j \chi_{ij} (\hat{\mathbf{w}}_j - \mathbf{w}_i)$ .

We consider two quantization schemes: the low precision quantizer (LPQ, see [32, Example 2]) and the cross-polytope vector quantization (VQ) technique [44], LPQ normalizes  $\mathbf{w}_i$  by  $\|\mathbf{w}_i\|_\infty$ , and then quantizes each component of  $\mathbf{w}_i/\|\mathbf{w}_i\|_\infty \in [-1, 1]^d$  with  $b$  bits using dithered quantization. The overall payload is  $B=64+b \cdot d$  bits, including the magnitude  $\|\mathbf{w}_i\|_\infty$  encoded with machine precision (64 bits). VQ is used with REP repetitions to reduce the variance of the quantization noise. Since the cross-polytope codebook contains  $2d$  codewords, the overall payload including repetitions is  $B=\text{REP}[\log_2(2d)]$ . The free parameters (number of subcarriers  $SC_n$  per node, bits for LPQ, repetitions for VQ) are optimized numerically for best performance. *The constant consensus and learning stepsizes are also optimized numerically, hence may not satisfy the stringent conditions of [32].* Since one OFDM symbol fits  $\frac{SC}{SC_n}$  transmissions, the frame duration is  $T=N \cdot \frac{SC_n}{SC} \cdot T_{\text{ofdm}}$ .

- *AirComp-D2D*, inspired by [18], leverages AirComp to efficiently solve DGD over device-to-device mesh networks. It organizes the network into non-interfering, star-based sub-networks via graph-coloring, scheduling multiple such sub-networks simultaneously to enhance spectral efficiency. Each sub-network operates in paired slots: in the first, the central node receives coherently aggregated models from neighbors via AirComp with channel inversion; in the second, it broadcasts its own model to its neighbors. This process continues until all D2D links have been activated. We generate the mesh network based on a maximum distance criterion, i.e. nodes  $i, j$  are connected if and only if they are less than  $\text{dist}_{\max}$  apart. We use the Metropolis-Hastings rule to design the mixing weights  $\omega_{ij}$  [53]. While [18] assumes Rayleigh flat-fading channels with no interference between non-neighboring devices, our adaptation extends to frequency-selective channels and accounts for interference. Note that *AirComp-D2D* requires CSI for power control, relies on *instantaneous* channel reciprocity for channel inversion, and requires centralized

knowledge of the graph topology for graph-coloring. In contrast, NCOTA-DGD does not require any such knowledge, and relies only on *average* (vs *instantaneous*) reciprocity,  $\Lambda_{ij}=\Lambda_{ji}$ . The free parameters ( $\text{dist}_{\max}$ , stepsizes) are optimized numerically for best performance. We refer to [18] for further details.

- *AirComp-FL*, based on [7], solves  $\{\mathbf{P}\}$  via FL across a star topology, with one node acting as the parameter server (PS, the star center). The process unfolds in three stages: first, the PS sends the current model to the  $N-1$  edge devices; then, each device updates this model via *local gradient descent*; finally, all devices simultaneously send their updates to the PS using AirComp with channel inversion, so that the latter updates the model for the next round. Like [18], this approach relies on instantaneous channel reciprocity and CSI, obtained by broadcasting an OFDM pilot symbol in the downlink.

- *Local only*: Nodes optimize independently using their datasets, without inter-node communication. This scheme illustrates the need for communication to solve the ML task: it results in a 90% test error, as shown in Fig. 5.c.

In Fig. 5, we compare these schemes versus the number of nodes  $N$ , after  $T_{\text{sim}}=2000\text{ms}$  of execution time. Note that the number of iterations completed by a certain scheme is  $\sim T_{\text{sim}}/T$ , function of its frame duration  $T$ , shown in Fig. 5.d. In addition to the normalized error (a), we also evaluate the *suboptimality gap* of the average model  $\bar{\mathbf{w}} = \frac{1}{N} \sum_i \mathbf{w}_i$ ,  $F(\bar{\mathbf{w}}) - F(\mathbf{w}^*)$  (b) and the *test error*  $\text{TEST}(\bar{\mathbf{w}})$ , computed on a test set of 1000 examples (100 for each class). For a parameter vector  $\mathbf{w}^\top = [\mathbf{w}^{(1)\top}, \dots, \mathbf{w}^{(9)\top}] \in \mathbb{R}^d$  and  $\mathbf{w}^{(0)}=\mathbf{0}$ , we predict the class associated to feature vector  $\mathbf{d}$  as  $\arg \max_c \bar{\mathbf{w}}^{(c)\top} \mathbf{d}$ . The results are further averaged over 20 algorithm trajectories generated through independent realizations of network deployment, channels, AWGN noise, and randomness used by each algorithm.

Overall, we observe that smaller normalized error typically translates to smaller suboptimality gap and test error. NCOTA-DGD performs the best when  $N \geq 100$ , under both spatially-i.i.d. and -dependent label scenarios. In fact, it executes the most iterations (Fig. 5.d) within the execution time  $T_{\text{sim}}$ , revealing its scalability to dense network deployments; in contrast, all other schemes, with the exception of *AirComp-FL* and *AirComp-D2D*, execute less iterations as  $N$  increases, due to the increased scheduling overhead. For smaller networks ( $N < 100$ ), *QDGD-LPQ* performs the best: in this regime, it schedules all devices within a small frame duration, yet it has better noise control through the use of digital transmissions, and avoids interference via OFDMA scheduling.

*AirComp-D2D* performs well across  $N$  in the spatially-

i.i.d. label scenario (between 3k and 6k iterations across all  $N$ , see Fig. 5.d), thanks to its efficient scheduling and the use of AirComp allowing simultaneous transmissions [18]. Yet, it performs poorly in the spatially-dependent label scenario, due to the slower propagation of information across the network, noted in the evaluations of Sec. V-A. With *AirComp-D2D*, information propagation is further hampered by the D2D connectivity structure, so that it takes several iterations for the information generated by the nodes at the edge to propagate through the mesh network to the rest of the network. In contrast, NCOTA-DGD does not rely on a predetermined D2D mesh network: it exploits the channel propagation conditions in the consensus phase, resulting in a much smaller performance degradation.

*AirComp-FL* also exhibits scalability with respect to  $N$  through AirComp. Yet, its effectiveness is limited by channel estimation errors and the star topology's vulnerability to path loss, especially affecting edge devices. This results in a communication bottleneck: uplink transmissions must accommodate the worst channel conditions to satisfy power constraints during channel inversion; in the downlink, transmission rates are reduced to guarantee reception by the edge devices. Conversely, NCOTA-DGD is topology-agnostic and leverages the local connectivity structure, achieving more robust performance for edge devices.

## VI. CONCLUSIONS

This paper presents a novel DGD algorithm tailored to wireless systems, addressing the challenges posed by noise, fading, and limited bandwidth without requiring inter-agent coordination, topology, or channel state information. Our approach, centered around a Non-Coherent Over-The-Air (NCOTA) consensus mechanism, leverages a noisy energy superposition property of wireless channels, allowing simultaneous, uncoordinated transmissions. This novel method achieves efficient consensus estimation without explicit mixing weights, exploiting path loss and adapting to a variety of fading and channel conditions. We prove that the error of NCOTA-DGD vanishes with rate  $\mathcal{O}(k^{-1/2})$  after  $k$  iterations, using suitably tuned consensus and learning stepsizes. Our results indicate a promising direction for decentralized optimization in wireless environments, showcasing faster convergence and operational efficiency, especially in dense networks. There are still open challenges in designing communication-efficient decentralized learning algorithms for wireless systems. These challenges include non-convex objectives and high model dimensionality, both inherent to deep neural network architectures. This work paves the way for further research in these areas.

*Acknowledgments:* Special thanks to Prof. Gesualdo Scutari for valuable discussions during manuscript preparation.

### APPENDIX A: BOUND ON THE SGD VARIANCE

**Lemma 5.** Assume  $|\mathcal{D}_i|=D \geq 2$ ,  $\forall i$  and minibatch gradients with minibatch size  $|\mathcal{B}_{ik}|=B \in \{1, \dots, D\}$ ,  $\forall i, k$ . Assume that: {1} the loss function  $\phi(\boldsymbol{\xi}; \mathbf{w})$  is  $\mu$  strongly-convex and  $L$  smooth with respect to  $\mathbf{w}$  (implying Assumption 2); {2}  $\|\nabla\phi(\boldsymbol{\xi}; \mathbf{w}^*)\| \leq \nabla^*$ ,  $\forall \boldsymbol{\xi} \in \mathcal{D}_i, \forall i$  (implying Def. 3). Then,

$$\frac{1}{N} \mathbb{E}[\|\boldsymbol{\epsilon}_k^{(2)}\|^2 | \mathcal{F}_k] \leq \frac{D-B}{B(D-1)} (\nabla^* + L \cdot \text{dm}(\mathcal{W}))^2 \triangleq \Sigma^{(2)}.$$

*Proof.* It directly follows from [54, Prop. 1], along with  $\|\nabla\phi(\boldsymbol{\xi}; \mathbf{w})\| \leq \|\nabla\phi(\boldsymbol{\xi}; \mathbf{w}^*)\| + \|\nabla\phi(\boldsymbol{\xi}; \mathbf{w}) - \nabla\phi(\boldsymbol{\xi}; \mathbf{w}^*)\| \leq \nabla^* + L\|\mathbf{w} - \mathbf{w}^*\| \leq \nabla^* + L \cdot \text{dm}(\mathcal{W})$ .  $\square$

### APPENDIX B: PROOF OF THEOREM 3

We prove (33)-(35) in appendices B.I-B.III, using the auxiliary lemmas in B.IV. We denote the set of semidefinite-positive  $n \times n$  matrices with eigenvalues in the interval  $[\mu, L]$  as  $\mathcal{S}_{\mu, L}^n$ . We start with two important properties.

**P1:** For any twice-differentiable function  $f: \mathbb{R}^n \mapsto \mathbb{R}$ ,  $\mu$ -strongly convex and  $L$ -smooth, we can express  $\nabla f(\mathbf{y})$  as the line integral of the Hessian matrix  $\nabla^2 f$  between  $\mathbf{x}$  and  $\mathbf{y}$ :

$$\begin{aligned} \nabla f(\mathbf{y}) &= \nabla f(\mathbf{x}) + \int_0^1 \nabla^2 f(\mathbf{x} + t(\mathbf{y} - \mathbf{x})) dt (\mathbf{y} - \mathbf{x}), \\ &= \nabla f(\mathbf{x}) + \mathbf{A}(\mathbf{y} - \mathbf{x}), \end{aligned} \quad (45)$$

where  $\mathbf{A}$  (function of  $\mathbf{x}, \mathbf{y}$ ) is the *mean Hessian* matrix between points  $\mathbf{x}$  and  $\mathbf{y}$ . Since  $f$  is  $\mu$ -strongly convex and  $L$ -smooth, it follows that  $\nabla^2 f \in \mathcal{S}_{\mu, L}^n$ , hence  $\mathbf{A} \in \mathcal{S}_{\mu, L}^n$ .

**P2:** For any function  $h: \mathbb{R}^n \mapsto \mathbb{R}$ ,  $\mu_h$ -strongly convex and  $L_h$ -smooth ( $L_h \geq \mu_h$ ), any  $\mathbf{x}, \mathbf{y} \in \mathbb{R}^n$ , and stepsize  $\eta \in [0, \frac{2}{\mu_h + L_h}]$ ,

$$\|(\mathbf{x} - \mathbf{y}) - \eta(\nabla h(\mathbf{x}) - \nabla h(\mathbf{y}))\| \leq (1 - \eta\mu_h)\|\mathbf{x} - \mathbf{y}\|. \quad (46)$$

To show this, use (45) to express  $\nabla h(\mathbf{y}) = \nabla h(\mathbf{x}) + \mathbf{A}(\mathbf{y} - \mathbf{x})$ , for some  $\mathbf{A} \in \mathcal{S}_{\mu_h, L_h}^n$ , hence

$$(\mathbf{x} - \mathbf{y}) - \eta(\nabla h(\mathbf{x}) - \nabla h(\mathbf{y})) = (\mathbf{I} - \eta\mathbf{A})(\mathbf{x} - \mathbf{y}).$$

Since  $\mathbf{A} \in \mathcal{S}_{\mu_h, L_h}^n$ , we further bound

$$\|(\mathbf{I} - \eta\mathbf{A})(\mathbf{x} - \mathbf{y})\|^2 \leq \max_{\rho \in [\mu_h, L_h]} (1 - \eta\rho)^2 \|\mathbf{x} - \mathbf{y}\|^2.$$

It is straightforward to show that the right-hand-side is maximized by  $\rho = \mu_h$  under the stepsize assumption, yielding (46).

#### Appendix B.I: Proof of (33)

Using the non-expansive property of projections (see, for instance, [55]), we can bound  $\|\mathbf{W}_{k+1} - \tilde{\mathbf{W}}_{k+1}\|^2$

$$\leq \|\mathbf{W}_k - \tilde{\mathbf{W}}_k - \eta_k(\nabla G_k(\mathbf{W}_k) - \nabla G_k(\tilde{\mathbf{W}}_k)) + \gamma_k \boldsymbol{\epsilon}_k^{(1)} - \eta_k \boldsymbol{\epsilon}_k^{(2)}\|^2.$$

Taking the expectation conditional on  $\mathcal{F}_k$  and using the independence of  $\boldsymbol{\epsilon}_k^{(1)}$  and  $\boldsymbol{\epsilon}_k^{(2)}$ , it follows  $\mathbb{E}[\|\mathbf{W}_{k+1} - \tilde{\mathbf{W}}_{k+1}\|^2 | \mathcal{F}_k]$

$$\leq \|(\mathbf{W}_k - \tilde{\mathbf{W}}_k) - \eta_k(\nabla G_k(\mathbf{W}_k) - \nabla G_k(\tilde{\mathbf{W}}_k))\|^2 \quad (47)$$

$$+ \gamma_k^2 N \Sigma^{(1)} + \eta_k^2 N \Sigma^{(2)}. \quad (48)$$

Note that Assumption 2 implies that  $G_k$  is  $\mu$ -strongly convex and  $L_{Gk} \triangleq L + \frac{\gamma_k}{\eta_k} \rho_N$ -smooth. Then, using (46), we find that (47)  $\leq (1 - \mu\eta_k)^2 \|\mathbf{W}_k - \tilde{\mathbf{W}}_k\|^2$ , as long as  $\eta_k \leq 2/(\mu + L_{Gk})$  (C1 of Theorem 3). Using this bound and computing the unconditional expectation, it follows  $\|\mathbf{W}_{k+1} - \tilde{\mathbf{W}}_{k+1}\|_{\mathbb{E}}^2$

$$\leq (1 - \mu\eta_k)^2 \|\mathbf{W}_k - \tilde{\mathbf{W}}_k\|_{\mathbb{E}}^2 + \gamma_k^2 N \Sigma^{(1)} + \eta_k^2 N \Sigma^{(2)}.$$

The result follows by induction and noting that  $\mathbf{W}_{\bar{k}} = \tilde{\mathbf{W}}_{\bar{k}}$ .

#### Appendix B.II: Proof of (35)

Let  $\hat{\mathbf{W}}_k \triangleq \arg \min_{\mathbf{W} \in \mathbb{R}^{Nd}} G_k(\mathbf{W})$  be the *unconstrained* minimizer of  $G_k$ ,<sup>13</sup> this is in contrast to  $\mathbf{W}_k^*$ , which minimizes

<sup>13</sup>Here, we assume that all  $f_i$ 's are defined on  $\mathbb{R}^d$ , and the extended functions are  $L$ -smooth and  $\mu$ -strongly convex on  $\mathbb{R}^d$ .

it over  $\mathcal{W}^N$ . In the last part of the proof, we will show that, when  $\frac{\eta_k}{\gamma_k} \leq \frac{\zeta \mu \rho_2}{\sqrt{N} \nabla^* L}$  (C2 of Theorem 3),  $\mathbf{W}_k^*$  and  $\hat{\mathbf{W}}_k$  coincide.

Since  $G_k$  is strongly-convex and smooth on  $\mathbb{R}^{Nd}$ ,  $\hat{\mathbf{W}}_k$  is the unique solution of  $\nabla G_k(\hat{\mathbf{W}}_k) = \mathbf{0}$  in  $\mathbb{R}^{Nd}$ . We now bound the distance of  $\hat{\mathbf{W}}_k$  from  $\mathbf{W}^*$ . From (45) with  $\mathbf{x} = \mathbf{W}^*$ ,  $\mathbf{y} = \hat{\mathbf{W}}_k$ , there exists  $\mathbf{A} \in \mathcal{S}_{\mu, L}^{Nd}$  such that

$$\nabla f(\hat{\mathbf{W}}_k) = \nabla f(\mathbf{W}^*) + \mathbf{A}(\hat{\mathbf{W}}_k - \mathbf{W}^*).$$

It follows that  $\mathbf{0} = \nabla G_k(\hat{\mathbf{W}}_k) - \frac{\gamma_k}{\eta_k} \hat{\mathbf{L}} \mathbf{W}^*$

$$= \nabla f(\hat{\mathbf{W}}_k) + \frac{\gamma_k}{\eta_k} \hat{\mathbf{L}}(\hat{\mathbf{W}}_k - \mathbf{W}^*) = \nabla f(\mathbf{W}^*) + \mathbf{B}(\hat{\mathbf{W}}_k - \mathbf{W}^*),$$

where we used  $\hat{\mathbf{L}} \mathbf{W}^* = (\mathbf{L} \otimes \mathbf{I}_d) \cdot (\mathbf{1}_N \otimes \mathbf{w}^*) = (\mathbf{L} \cdot \mathbf{1}_N) \otimes \mathbf{w}^* = \mathbf{0}$ , and defined  $\mathbf{B} \triangleq \mathbf{A} + \frac{\gamma_k}{\eta_k} \hat{\mathbf{L}} \succeq \mu \mathbf{I}$ . Solving with respect to  $\hat{\mathbf{W}}_k - \mathbf{W}^*$  and computing the norm of both sides, we find

$$\|\hat{\mathbf{W}}_k - \mathbf{W}^*\| = \|\mathbf{B}^{-1} \nabla f(\mathbf{W}^*)\|. \quad (49)$$

Note that  $\nabla f(\mathbf{W}^*) \perp (\mathbf{1}_N \otimes \mathbf{I}_d)$  (in fact,  $\sum_i \nabla f_i(\mathbf{w}^*) = \mathbf{0}$  from the optimality condition on  $\mathbf{w}^*$ , since  $\mathbf{w}^* \in \text{int}(\mathcal{W})$ ). Hence, we bound (49) via Lemma 6 in B.IV with  $U = \frac{\gamma_k}{\eta_k}$  as

$$\|\hat{\mathbf{W}}_k - \mathbf{W}^*\| \leq \frac{L}{\mu \rho_2} \frac{\eta_k}{\gamma_k} \|\nabla f(\mathbf{W}^*)\| \leq \frac{\sqrt{N} \nabla^* L \eta_k}{\mu \rho_2 \gamma_k}, \quad (50)$$

where in the last step we used  $\|\nabla f(\mathbf{W}^*)\| \leq \sqrt{\sum_i \|\nabla f_i(\mathbf{w}^*)\|^2} \leq \sqrt{N} \nabla^*$  from Definition 3.

Next, we show that  $\hat{\mathbf{W}}_k \in \mathcal{W}^N$ , hence it coincides with the solution of the constrained problem ( $\hat{\mathbf{W}}_k = \mathbf{W}_k^*$ ). Since  $\mathbf{w}^*$  is at distance  $\zeta$  from the boundary of  $\mathcal{W}$  (Assumption 3), it suffices to show that  $\|\hat{\mathbf{w}}_{ik} - \mathbf{w}^*\| \leq \zeta$ ,  $\forall i$  (i.e.,  $\mathbf{w}^*$  is closer to  $\hat{\mathbf{w}}_{ik}$  than to the boundary of  $\mathcal{W}$ ). Indeed,  $\|\hat{\mathbf{w}}_{ik} - \mathbf{w}^*\| \leq \|\hat{\mathbf{W}}_k - \mathbf{W}^*\| \leq \frac{\sqrt{N} \nabla^* L \eta_k}{\mu \rho_2 \gamma_k}$ , hence, when  $\frac{\eta_k}{\gamma_k} \leq \frac{\zeta \mu \rho_2}{\sqrt{N} \nabla^* L}$  (C2 of Theorem 3), it follows that  $\hat{\mathbf{W}}_k = \mathbf{W}_k^*$  and

$$\nabla G_k(\mathbf{W}_k^*) = \mathbf{0}, \quad (51)$$

and (35) readily follows from (50).

### Appendix B.III: Proof of (34)

Using the triangle inequality, we bound

$$\|\tilde{\mathbf{W}}_{k+1} - \mathbf{W}_{k+1}^*\| \leq \|\tilde{\mathbf{W}}_{k+1} - \mathbf{W}_k^*\| + \|\mathbf{W}_{k+1}^* - \mathbf{W}_k^*\|. \quad (52)$$

Using the fixed point optimality condition  $\mathbf{W}_k^* = \Pi^N[\mathbf{W}_k^* - \eta \nabla G_k(\mathbf{W}_k^*)]$ ,  $\forall \eta \geq 0$  and the non-expansive property of projections [55], we bound the first term of (52) as  $\|\tilde{\mathbf{W}}_{k+1} - \mathbf{W}_k^*\|$

$$\begin{aligned} &= \|\Pi^N[\tilde{\mathbf{W}}_k - \eta_k \nabla G_k(\tilde{\mathbf{W}}_k)] - \Pi^N[\mathbf{W}_k^* - \eta_k \nabla G_k(\mathbf{W}_k^*)]\| \\ &\leq \|\tilde{\mathbf{W}}_k - \mathbf{W}_k^* - \eta_k (\nabla G_k(\tilde{\mathbf{W}}_k) - \nabla G_k(\mathbf{W}_k^*))\| \\ &\leq (1 - \mu \eta_k) \|\tilde{\mathbf{W}}_k - \mathbf{W}_k^*\|, \end{aligned} \quad (53)$$

where in the last step we used (46) since  $G_k$  is  $\mu$ -strongly convex and  $L_{G_k} \triangleq L + \frac{\gamma_k}{\eta_k} \rho_N$ -smooth, provided that  $\eta_k \leq 2/(\mu + L_{G_k})$  (C1 of Theorem 3). We now bound  $\|\mathbf{W}_{k+1}^* - \mathbf{W}_k^*\|$ . First, note that, for  $t \geq \bar{k}$ ,  $\mathbf{W}_t^*$  satisfies the optimality condition  $\nabla G_t(\mathbf{W}_t^*) = \mathbf{0}$  (see (51)). It then follows that

$$\mathbf{0} = \nabla G_{k+1}(\mathbf{W}_{k+1}^*) = \nabla f(\mathbf{W}_{k+1}^*) + \frac{\gamma_{k+1}}{\eta_{k+1}} \hat{\mathbf{L}} \mathbf{W}_{k+1}^*, \quad (54)$$

$$\mathbf{0} = \nabla G_k(\mathbf{W}_k^*) = \nabla f(\mathbf{W}_k^*) + \frac{\gamma_k}{\eta_k} \hat{\mathbf{L}} \mathbf{W}_k^*. \quad (55)$$

Furthermore, from (45) with  $\mathbf{x} = \mathbf{W}_k^*$  and  $\mathbf{y} = \mathbf{W}_{k+1}^*$ , there exists  $\mathbf{A} \in \mathcal{S}_{\mu, L}^{Nd}$  such that  $\nabla f(\mathbf{W}_{k+1}^*) = \nabla f(\mathbf{W}_k^*) +$

$\mathbf{A}(\mathbf{W}_{k+1}^* - \mathbf{W}_k^*)$ . We use this expression in (54), subtract (55), reorganize and solve. These steps yield

$$\mathbf{W}_{k+1}^* - \mathbf{W}_k^* = - \left( \frac{\gamma_{k+1}}{\eta_{k+1}} - \frac{\gamma_k}{\eta_k} \right) \mathbf{B}^{-1} \hat{\mathbf{L}} \mathbf{W}_{k+1}^*,$$

where  $\mathbf{B} \triangleq \mathbf{A} + \frac{\gamma_k}{\eta_k} \hat{\mathbf{L}}$ . Therefore,

$$\|\mathbf{W}_{k+1}^* - \mathbf{W}_k^*\| \leq \left( \frac{\gamma_{k+1}}{\eta_{k+1}} - \frac{\gamma_k}{\eta_k} \right) \|\mathbf{B}^{-1} \hat{\mathbf{L}} \mathbf{W}_{k+1}^*\|. \quad (56)$$

Noting that  $\hat{\mathbf{L}} \mathbf{W}_{k+1}^* \perp (\mathbf{1}_N \otimes \mathbf{I}_d)$  (since  $\mathbf{L} \cdot \mathbf{1} = \mathbf{0}$ ), we use Lemma 6 in B.IV with  $U = \frac{\gamma_k}{\eta_k}$  to bound

$$\|\mathbf{W}_{k+1}^* - \mathbf{W}_k^*\| \leq \frac{L}{\mu \rho_2} \left( \frac{\gamma_{k+1}}{\eta_{k+1}} - \frac{\gamma_k}{\eta_k} \right) \frac{\eta_k}{\gamma_k} \|\hat{\mathbf{L}} \mathbf{W}_{k+1}^*\|.$$

Finally, we bound  $\|\hat{\mathbf{L}} \mathbf{W}_{k+1}^*\|$  via Lemma 7 in Appendix B.IV:

$$\|\mathbf{W}_{k+1}^* - \mathbf{W}_k^*\| \leq \left( \frac{\eta_k}{\gamma_k} - \frac{\eta_{k+1}}{\gamma_{k+1}} \right) \frac{\sqrt{N} \nabla^* L}{\mu \rho_2} \left( 1 + \frac{L^2}{\mu \rho_2} \frac{\eta_k}{\gamma_k} \right).$$

Eq. (34) follows by combining this result with (53) into (52), and solving via induction with  $\|\tilde{\mathbf{W}}_{\bar{k}} - \mathbf{W}_{\bar{k}}^*\| \leq \sqrt{N} \text{dm}(\mathcal{W})$ .

### Appendix B.IV: Auxiliary lemmas

**Lemma 6.** Let  $\mathbf{B} = \mathbf{A} + U \hat{\mathbf{L}}$ , where  $U > 0$ ,  $\mathbf{A} \in \mathcal{S}_{\mu, L}^{Nd}$ . Then,

$$\|\mathbf{B}^{-1} \mathbf{v}\| \leq \frac{1}{U} \cdot \frac{L}{\mu \rho_2} \|\mathbf{v}\|, \quad \forall \mathbf{v} \perp (\mathbf{1}_N \otimes \mathbf{I}_d).$$

*Proof.* Using  $\mathbf{A} \succeq \mu \mathbf{I}$ , we start with bounding

$$\|\mathbf{B}^{-1} \mathbf{v}\| = \|\mathbf{A}^{-1} \mathbf{A} \mathbf{B}^{-1} \mathbf{v}\| \leq \frac{1}{\mu} \|\mathbf{A} \mathbf{B}^{-1} \mathbf{v}\|. \quad (57)$$

Let  $\mathbf{L} = \mathbf{V} \mathbf{\Lambda} \mathbf{V}^\top$  be the eigenvalue decomposition of the Laplacian matrix, where  $\mathbf{V}$  is unitary and  $\mathbf{\Lambda}$  is diagonal. Since  $\mathbf{L} \cdot \mathbf{1} = \mathbf{0}$ , the first column of  $\mathbf{V}$  equals  $\mathbf{1}_N / \sqrt{N}$  and  $[\mathbf{\Lambda}]_{1,1} = 0$ ; furthermore,  $[\mathbf{\Lambda}]_{i,i} \geq \rho_2 > 0, \forall i > 1$  (Assumption 4). Then,  $\hat{\mathbf{L}} = \mathbf{L} \otimes \mathbf{I}_d = \hat{\mathbf{V}} \hat{\mathbf{\Lambda}} \hat{\mathbf{V}}^\top$ , where  $\hat{\mathbf{V}} = \mathbf{V} \otimes \mathbf{I}_d$  and  $\hat{\mathbf{\Lambda}} = \mathbf{\Lambda} \otimes \mathbf{I}_d$ . Let

$$\tilde{\mathbf{A}} = \hat{\mathbf{V}}^\top \mathbf{A} \hat{\mathbf{V}} = \begin{bmatrix} \tilde{\mathbf{A}}_{1,1} & \tilde{\mathbf{A}}_{1,2} \\ \tilde{\mathbf{A}}_{1,2}^\top & \tilde{\mathbf{A}}_{2,2} \end{bmatrix}, \quad \hat{\mathbf{\Lambda}} = \begin{bmatrix} \mathbf{0} & \mathbf{0} \\ \mathbf{0} & \hat{\mathbf{\Lambda}}_{2,2} \end{bmatrix},$$

where  $\tilde{\mathbf{A}}_{1,1} \in \mathbb{R}^{d \times d}$ ,  $\tilde{\mathbf{A}}_{1,2} \in \mathbb{R}^{d \times (N-1)d}$ ,  $\tilde{\mathbf{A}}_{2,2}$  and  $\hat{\mathbf{\Lambda}}_{2,2} \in \mathbb{R}^{(N-1)d \times (N-1)d}$  with  $\hat{\mathbf{\Lambda}}_{2,2} \succeq \rho_2 \mathbf{I}$ . Since  $\mathbf{v} \perp (\mathbf{1}_N \otimes \mathbf{I}_d)$ , we also define  $\hat{\mathbf{V}}^\top \mathbf{v} = [\mathbf{0}^\top, \mathbf{x}^\top]^\top$  for suitable  $\mathbf{x}$ . Therefore,

$$\|\mathbf{A} \mathbf{B}^{-1} \mathbf{v}\| = \left\| \tilde{\mathbf{A}} (\tilde{\mathbf{A}} + U \hat{\mathbf{\Lambda}})^{-1} \begin{bmatrix} \mathbf{0} \\ \mathbf{x} \end{bmatrix} \right\|.$$

Using the inversion properties of  $2 \times 2$  block matrices and simplifying, we continue as  $\|\mathbf{A} \mathbf{B}^{-1} \mathbf{v}\|$

$$= \left\| \begin{bmatrix} \tilde{\mathbf{A}}_{1,1} & \tilde{\mathbf{A}}_{1,2} \\ \tilde{\mathbf{A}}_{1,2}^\top & \tilde{\mathbf{A}}_{2,2} \end{bmatrix} \begin{bmatrix} \bullet & -\tilde{\mathbf{A}}_{1,1}^{-1} \tilde{\mathbf{A}}_{1,2} \mathbf{S}_U^{-1} \\ \bullet & \mathbf{S}_U^{-1} \end{bmatrix} \begin{bmatrix} \mathbf{0} \\ \mathbf{x} \end{bmatrix} \right\| = \|\mathbf{S}_0 \mathbf{S}_U^{-1} \mathbf{x}\|,$$

where  $\mathbf{S}_z \triangleq \tilde{\mathbf{A}}_{2,2} - \tilde{\mathbf{A}}_{1,2}^\top \tilde{\mathbf{A}}_{1,1}^{-1} \tilde{\mathbf{A}}_{1,2} + z \hat{\mathbf{\Lambda}}$  is the Schur complement of block  $\tilde{\mathbf{A}}_{1,1}$  of  $\tilde{\mathbf{A}} + z \hat{\mathbf{\Lambda}}$ , and the block elements  $\bullet$  are irrelevant, being then multiplied by  $\mathbf{0}$ . Using the facts that  $\mathbf{0} \prec \mathbf{S}_0 \leq L \cdot \mathbf{I}$  ( $\mathbf{S}_0^{-1}$  is the lower-diagonal block of  $\tilde{\mathbf{A}}^{-1}$ , and  $\tilde{\mathbf{A}}^{-1} \succeq \frac{1}{L} \mathbf{I}$ ) and  $\mathbf{S}_U = \mathbf{S}_0 + U \hat{\mathbf{\Lambda}} \succeq U \rho_2 \mathbf{I}$ , yield

$$\|\mathbf{A} \mathbf{B}^{-1} \mathbf{v}\| = \|\mathbf{S}_0 \mathbf{S}_U^{-1} \mathbf{x}\| \leq L \|\mathbf{S}_U^{-1} \mathbf{x}\| \leq \frac{L}{U \rho_2} \|\mathbf{x}\| = \frac{L}{U \rho_2} \|\mathbf{v}\|.$$

The final result is obtained by using this bound in (57).  $\square$



**Lemma 7.**  $\|\hat{\mathbf{L}}\mathbf{W}_k^*\| \leq \frac{\eta_k}{\gamma_k} \sqrt{N} \nabla^* \left(1 + \frac{L^2}{\mu\rho_2} \frac{\eta_k}{\gamma_k}\right), \forall k \geq \bar{\kappa}$ .

*Proof.* From the proof of (35) in Appendix B.II,  $\nabla G_k(\mathbf{W}_k^*) = \nabla f(\mathbf{W}_k^*) + \frac{\eta_k}{\eta_k} \hat{\mathbf{L}}\mathbf{W}_k^* = \mathbf{0}$  for  $k \geq \bar{\kappa}$  (see (51)). It follows that

$$\|\hat{\mathbf{L}}\mathbf{W}_k^*\| = \frac{\eta_k}{\gamma_k} \|\nabla f(\mathbf{W}_k^*)\|.$$

Moreover, using the triangle inequality and smoothness of  $f$ ,

$$\begin{aligned} \|\nabla f(\mathbf{W}_k^*)\| &\leq \|\nabla f(\mathbf{W}_k^*) - \nabla f(\mathbf{W}^*)\| + \|\nabla f(\mathbf{W}^*)\| \\ &\leq L\|\mathbf{W}_k^* - \mathbf{W}^*\| + \|\nabla f(\mathbf{W}^*)\|. \end{aligned}$$

The final result is obtained by bounding  $\|\mathbf{W}_k^* - \mathbf{W}^*\|$  as in (35), and using  $\|\nabla f(\mathbf{W}^*)\| \leq \sqrt{N} \nabla^*$ .  $\square$

#### APPENDIX C: PROOF OF THEOREM 4

*Proof.* First, note that the choice of stepsizes guarantees the existence of  $\bar{\kappa} \geq 0$  (finite) such that **C1-C3** are satisfied for  $k \geq \bar{\kappa}$ . Consider  $k \geq \bar{\kappa}$ . In the proof, we will often need

$$S_k^n(v) \triangleq \sum_{t=\bar{\kappa}}^{k-1} P_{tk}^n (1+\delta t)^{-v}, \text{ for } 1 \leq v \leq \frac{5}{4}n \text{ and } n \geq 1.$$

To bound  $S_k^n(v)$ , we first bound  $P_{tk}$  for  $t \geq \bar{\kappa} - 1$  as

$$\begin{aligned} P_{tk} &= \prod_{j=t+1}^{k-1} (1 - \mu\eta_j) \leq e^{-\mu\eta_0 \sum_{j=t+1}^{k-1} (1+\delta j)^{-1}} \\ &\leq e^{-\mu\eta_0 \int_{t+1}^k (1+\delta x)^{-1} dx} = (1+\delta k)^{-\frac{\mu\eta_0}{\delta}} (1+\delta(t+1))^{\frac{\mu\eta_0}{\delta}}. \end{aligned} \quad (58)$$

For  $t \geq \bar{\kappa}$ , we further bound  $(1+\delta(t+1))^{\frac{\mu\eta_0}{\delta}}$

$$= (1+\delta t)^{\frac{\mu\eta_0}{\delta}} \left(1 + \frac{\delta}{1+\delta t}\right)^{\frac{\mu\eta_0}{\delta}} \leq (1+\delta t)^{\frac{\mu\eta_0}{\delta}} \left(1 + \frac{\delta}{1+\delta\bar{\kappa}}\right)^{\frac{\mu\eta_0}{\delta}};$$

using  $1+x \leq e^x$ , we further bound the last term above as

$$\left(1 + \frac{\delta}{1+\delta\bar{\kappa}}\right)^{\frac{\mu\eta_0}{\delta}} \leq e^{\mu\eta_0/(1+\delta\bar{\kappa})} = e^{\mu\eta_{\bar{\kappa}}} \leq e,$$

where in the last step we used  $\eta_{\bar{\kappa}} \leq 2/(\mu+L) \leq 1/\mu$  from **C1** of Theorem 3. It follows that  $P_{tk} \leq e(1+\delta k)^{-\frac{\mu\eta_0}{\delta}} (1+\delta t)^{\frac{\mu\eta_0}{\delta}}$  for  $t \geq \bar{\kappa}$ . Using this bound in  $S_k^n(v)$ , we obtain

$$S_k^n(v) \leq e^n (1+\delta k)^{-n\frac{\mu\eta_0}{\delta}} \sum_{t=\bar{\kappa}}^{k-1} (1+\delta t)^{n\frac{\mu\eta_0}{\delta}-v}.$$

Since  $n\frac{\mu\eta_0}{\delta} \geq 5/4n \geq v$ , we continue as

$$\begin{aligned} S_k^n(v) &\leq e^n (1+\delta k)^{-n\frac{\mu\eta_0}{\delta}} \int_{\bar{\kappa}}^k (1+\delta x)^{n\frac{\mu\eta_0}{\delta}-v} dx \\ &\leq \frac{e^n}{n\mu\eta_0 - \delta(v-1)} (1+\delta k)^{-v+1} \leq \frac{5e^n}{4\mu\eta_0} (1+\delta k)^{-v+1}, \end{aligned} \quad (59)$$

where the last step used  $\delta \leq \frac{4}{5}\mu\eta_0$  and  $v \leq 5/4n$ .

With  $\gamma_k, \eta_k$  as in Theorem 4, we specialize (33) as

$$\frac{1}{N} \|\mathbf{W}_k - \tilde{\mathbf{W}}_k\|_{\mathbb{E}}^2 \leq \gamma_0^2 \Sigma^{(1)} S_k^2(3/2) + \eta_0^2 \Sigma^{(2)} S_k^2(2).$$

The bound in (40) follows using (59) and  $\sqrt{a+b} \leq \sqrt{a} + \sqrt{b}$  for  $a, b \geq 0$ . Similarly, we specialize (34) as

$$\frac{1}{\sqrt{N}} \|\tilde{\mathbf{W}}_k - \mathbf{W}_k^*\|_{\mathbb{E}} \leq \text{dm}(\mathcal{W}) \cdot P_{(\bar{\kappa}-1)k} + \frac{\nabla^* L \eta_0}{\mu\rho_2 \gamma_0} \sum_{t=\bar{\kappa}}^{k-1} P_{tk}$$

$$\times \left(1 + \frac{L^2}{\mu\rho_2 \gamma_0} \eta_0 (1+\delta t)^{-1/4}\right) \left((1+\delta t)^{-1/4} - (1+\delta(t+1))^{-1/4}\right).$$

Since  $x^{-1/4}$  is convex for  $x > 0$ , we further bound  $(1+\delta(t+1))^{-1/4} \geq (1+\delta t)^{-1/4} - \delta/4(1+\delta t)^{-5/4}$ , hence

$$\begin{aligned} &\frac{1}{\sqrt{N}} \|\tilde{\mathbf{W}}_k - \mathbf{W}_k^*\|_{\mathbb{E}} \leq \text{dm}(\mathcal{W}) \cdot P_{(\bar{\kappa}-1)k} \\ &\quad + \frac{\nabla^* L \eta_0 \delta}{4\mu\rho_2 \gamma_0} \left(S_k^1(5/4) + \frac{L^2}{\mu\rho_2 \gamma_0} S_k^1(3/2)\right). \end{aligned}$$

The bound in (41) readily follows using (58), (59) and  $\delta \leq \frac{4}{5}\mu\eta_0$ . (42) follows by direct substitution into (35).  $\square$

#### REFERENCES

- [1] N. Michelusi, "Decentralized federated learning via non-coherent over-the-air consensus," in *ICC 2023 - IEEE International Conference on Communications*, 2023, pp. 3102–3107.
- [2] —, "Csi-free over-the-air decentralized learning over frequency selective channels," in *ICASSP 2024 - 2024 IEEE International Conference on Acoustics, Speech and Signal Processing (ICASSP)*, 2024, pp. 13 076–13 080.
- [3] S. Kar and J. M. Moura, "Consensus + innovations distributed inference over networks: cooperation and sensing in networked systems," *IEEE Signal Processing Magazine*, vol. 30, no. 3, pp. 99–109, 2013.
- [4] T. T. Doan, S. T. Maguluri, and J. Romberg, "Convergence Rates of Distributed Gradient Methods Under Random Quantization: A Stochastic Approximation Approach," *IEEE Transactions on Automatic Control*, vol. 66, no. 10, pp. 4469–4484, 2021.
- [5] A. Nedić, J.-S. Pang, G. Scutari, and Y. Sun, *Multi-agent Optimization*, 1st ed. Springer, Cham, 2018.
- [6] T. Yang, X. Yi, J. Wu, Y. Yuan, D. Wu, Z. Meng, Y. Hong, H. Wang, Z. Lin, and K. H. Johansson, "A survey of distributed optimization," *Annual Reviews in Control*, vol. 47, pp. 278–305, 2019.
- [7] G. Zhu, Y. Wang, and K. Huang, "Broadband Analog Aggregation for Low-Latency Federated Edge Learning," *IEEE Transactions on Wireless Communications*, vol. 19, no. 1, pp. 491–506, 2020.
- [8] X. Lian, C. Zhang, H. Zhang, C.-J. Hsieh, W. Zhang, and J. Liu., "Can decentralized algorithms outperform centralized algorithms? A case study for decentralized parallel stochastic gradient descent," in *Proc. 31st NeurIPS*, Dec. 2017.
- [9] Y. Xiao, Y. Ye, S. Huang, L. Hao, Z. Ma, M. Xiao, S. Mumtaz, and O. A. Dobre, "Fully Decentralized Federated Learning-Based On-Board Mission for UAV Swarm System," *IEEE Communications Letters*, vol. 25, no. 10, pp. 3296–3300, 2021.
- [10] S. Savazzi, M. Nicoli, and V. Rampa, "Federated Learning With Cooperating Devices: A Consensus Approach for Massive IoT Networks," *IEEE Internet of Things Journal*, vol. 7, no. 5, pp. 4641–4654, 2020.
- [11] A. Nedić and A. Ozdaglar, "Distributed subgradient methods for multi-agent optimization," *IEEE Trans. Autom. Control*, vol. 54, no. 1, pp. 48–61, Jan. 2009.
- [12] K. Yuan, Q. Ling, and W. Yin, "On the Convergence of Decentralized Gradient Descent," *SIAM Journal on Optimization*, vol. 26, no. 3, pp. 1835–1854, 2016.
- [13] R. Xin, S. Pu, A. Nedic, and U. A. Khan, "A general framework for decentralized optimization with first-order methods," *Proceedings of the IEEE*, vol. 108, no. 11, pp. 1869–1889, 2020.
- [14] N. Michelusi, G. Scutari, and C.-S. Lee, "Finite-Bit Quantization for Distributed Algorithms With Linear Convergence," *IEEE Transactions on Information Theory*, vol. 68, no. 11, pp. 7254–7280, 2022.
- [15] Y. Kajiyama, N. Hayashi, and S. Takai, "Linear convergence of consensus-based quantized optimization for smooth and strongly convex cost functions," *IEEE Transactions on Automatic Control*, vol. 66, no. 3, pp. 1254–1261, 2021.
- [16] S. Magnússon, H. Shokri-Ghadikolaei, and N. Li, "On maintaining linear convergence of distributed learning and optimization under limited communication," *IEEE Trans. Signal Process.*, vol. 68, pp. 6101–6116, Oct. 2020.
- [17] R. Saha, S. Rini, M. Rao, and A. J. Goldsmith, "Decentralized optimization over noisy, rate-constrained networks: Achieving consensus by communicating differences," *IEEE Journal on Selected Areas in Communications*, vol. 40, no. 2, pp. 449–467, 2022.

- [18] H. Xing, O. Simeone, and S. Bi, "Federated learning over wireless device-to-device networks: Algorithms and convergence analysis," *IEEE Journal on Selected Areas in Communications*, vol. 39, no. 12, pp. 3723–3741, 2021.
- [19] E. Ozfatura, S. Rini, and D. Gündüz, "Decentralized SGD with Over-the-Air Computation," in *GLOBECOM 2020 - 2020 IEEE Global Communications Conference*, 2020, pp. 1–6.
- [20] Y. Shi, Y. Zhou, and Y. Shi, "Over-the-air decentralized federated learning," in *2021 IEEE International Symposium on Information Theory (ISIT)*, 2021, pp. 455–460.
- [21] X. Chen, D. W. K. Ng, W. Yu, E. G. Larsson, N. Al-Dhahir, and R. Schober, "Massive Access for 5G and Beyond," *IEEE Journal on Selected Areas in Communications*, vol. 39, no. 3, pp. 615–637, 2021.
- [22] K. Rokade and R. K. Kalaimani, "Distributed computation of fast consensus weights using ADMM," *Automatica*, vol. 142, p. 110322, 2022.
- [23] C.-S. Lee, N. Michelusi, and G. Scutari, "Finite rate distributed weight-balancing and average consensus over digraphs," *IEEE Transactions on Automatic Control*, vol. 66, no. 10, pp. 4530–4545, 2021.
- [24] K. Yang, T. Jiang, Y. Shi, and Z. Ding, "Federated learning via over-the-air computation," *IEEE Transactions on Wireless Communications*, vol. 19, no. 3, pp. 2022–2035, 2020.
- [25] M. M. Amiri and D. Gündüz, "Federated learning over wireless fading channels," *IEEE Transactions on Wireless Communications*, vol. 19, no. 5, pp. 3546–3557, 2020.
- [26] M. M. Amiri, D. Gündüz, S. R. Kulkarni, and H. V. Poor, "Convergence of federated learning over a noisy downlink," *IEEE Transactions on Wireless Communications*, vol. 21, no. 3, pp. 1422–1437, 2022.
- [27] M. M. Amiri, T. M. Duman, D. Gündüz, S. R. Kulkarni, and H. V. Poor, "Blind federated edge learning," *IEEE Transactions on Wireless Communications*, vol. 20, no. 8, pp. 5129–5143, 2021.
- [28] M. Mohammadi Amiri and D. Gündüz, "Machine learning at the wireless edge: Distributed stochastic gradient descent over-the-air," *IEEE Transactions on Signal Processing*, vol. 68, pp. 2155–2169, 2020.
- [29] Z. Jiang, G. Yu, Y. Cai, and Y. Jiang, "Decentralized Edge Learning via Unreliable Device-to-Device Communications," *IEEE Transactions on Wireless Communications*, vol. 21, no. 11, pp. 9041–9055, 2022.
- [30] H. Ye, L. Liang, and G. Y. Li, "Decentralized Federated Learning With Unreliable Communications," *IEEE Journal of Selected Topics in Signal Processing*, vol. 16, no. 3, pp. 487–500, 2022.
- [31] E. Jeong, M. Zecchin, and M. Kountouris, "Asynchronous Decentralized Learning over Unreliable Wireless Networks," in *ICC 2022 - IEEE International Conference on Communications*, 2022, pp. 607–612.
- [32] A. Reiszadeh, A. Mokhtari, H. Hassani, and R. Pedarsani, "An exact quantized decentralized gradient descent algorithm," *IEEE Transactions on Signal Processing*, vol. 67, no. 19, pp. 4934–4947, 2019.
- [33] H. Xiao, K. Rasul, and R. Vollgraf, "Fashion-MNIST: a Novel Image Dataset for Benchmarking Machine Learning Algorithms," *CoRR*, vol. abs/1708.07747, 2017.
- [34] J. Tsitsiklis, D. Bertsekas, and M. Athans, "Distributed asynchronous deterministic and stochastic gradient optimization algorithms," *IEEE Transactions on Automatic Control*, vol. 31, no. 9, pp. 803–812, 1986.
- [35] H. Taheri, A. Mokhtari, H. Hassani, and R. Pedarsani, "Quantized decentralized stochastic learning over directed graphs," in *Proc. 37th ICML*, Jul. 2020.
- [36] D. Kovalev, A. Koloskova, M. Jaggi, P. Richtárik, and S. U. Stich, "A linearly convergent algorithm for decentralized optimization: Sending less bits for free!" in *Proc. 24th AISTATS*, Apr. 2021.
- [37] Y. Liao, Z. Li, K. Huang, and S. Pu, "A compressed gradient tracking method for decentralized optimization with linear convergence," *IEEE Trans. on Automatic Control*, vol. 67, no. 10, pp. 5622–5629, 2022.
- [38] M. Chen, D. Gündüz, K. Huang, W. Saad, M. Bennis, A. V. Feljan, and H. V. Poor, "Distributed learning in wireless networks: Recent progress and future challenges," *IEEE Journal on Selected Areas in Communications*, vol. 39, no. 12, pp. 3579–3605, 2021.
- [39] B. Nazer and M. Gastpar, "Computation Over Multiple-Access Channels," *IEEE Transactions on Information Theory*, vol. 53, no. 10, pp. 3498–3516, 2007.
- [40] J. Choi, "Communication-Efficient Distributed SGD Using Random Access for Over-the-Air Computation," *IEEE Journal on Selected Areas in Information Theory*, vol. 3, no. 2, pp. 206–216, 2022.
- [41] M. Faraz and N. Michelusi, "Biased Over-the-Air Federated Learning under Wireless Heterogeneity," in *IEEE International Conference on Communications (ICC)*, 2024.
- [42] J. Dong, Y. Shi, and Z. Ding, "Blind Over-the-Air Computation and Data Fusion via Provable Wirtinger Flow," *IEEE Transactions on Signal Processing*, vol. 68, pp. 1136–1151, 2020.
- [43] T. Sery and K. Cohen, "On Analog Gradient Descent Learning Over Multiple Access Fading Channels," *IEEE Transactions on Signal Processing*, vol. 68, pp. 2897–2911, 2020.
- [44] V. Gandikota, D. Kane, R. K. Maity, and A. Mazumdar, "vqSGD: Vector Quantized Stochastic Gradient Descent," *IEEE Transactions on Information Theory*, vol. 68, no. 7, pp. 4573–4587, 2022.
- [45] M. Chen, H. V. Poor, W. Saad, and S. Cui, "Wireless communications for collaborative federated learning," *IEEE Communications Magazine*, vol. 58, no. 12, pp. 48–54, 2020.
- [46] F. P.-C. Lin, S. Hosseinalipour, S. S. Azam, C. G. Brinton, and N. Michelusi, "Semi-Decentralized Federated Learning With Cooperative D2D Local Model Aggregations," *IEEE Journal on Selected Areas in Communications*, vol. 39, no. 12, pp. 3851–3869, 2021.
- [47] M. Yemini, R. Saha, E. Ozfatura, D. Gündüz, and A. J. Goldsmith, "Semi-decentralized federated learning with collaborative relaying," in *2022 IEEE International Symposium on Information Theory (ISIT)*, 2022, pp. 1471–1476.
- [48] S. Hosseinalipour, S. S. Azam, C. G. Brinton, N. Michelusi, V. Aggarwal, D. J. Love, and H. Dai, "Multi-Stage Hybrid Federated Learning Over Large-Scale D2D-Enabled Fog Networks," *IEEE/ACM Transactions on Networking*, vol. 30, no. 4, pp. 1569–1584, 2022.
- [49] A. Goldsmith, *Wireless Communications*. Cambridge University Press, 2005.
- [50] J. L. Gross, J. Yellen, and P. Zhang, *Handbook of Graph Theory, Second Edition*, 2nd ed. Chapman & Hall/CRC, 2013.
- [51] S. Wang, T. Tuor, T. Salonidis, K. K. Leung, C. Makaya, T. He, and K. Chan, "Adaptive Federated Learning in Resource Constrained Edge Computing Systems," *IEEE Journal on Selected Areas in Communications*, vol. 37, no. 6, pp. 1205–1221, 2019.
- [52] I. Florescu and C. A. Tudor, *Handbook of Probability*. Wiley, 2013.
- [53] V. Schwarz, G. Hannak, and G. Matz, "On the convergence of average consensus with generalized metropolis-hasting weights," in *IEEE International Conference on Acoustics, Speech and Signal Processing (ICASSP)*, 2014, pp. 5442–5446.
- [54] J. Wu, W. Hu, H. Xiong, J. Huan, V. Braverman, and Z. Zhu, "On the Noisy Gradient Descent that Generalizes as SGD," in *ICML*, 2020.
- [55] D. Bertsekas, A. Nedić, and A. Ozdaglar, *Convex Analysis and Optimization*. Athena Scientific, 2003.



**Nicolò Michelusi** (Senior Member, IEEE) received the B.Sc. (with honors), M.Sc. (with honors), and Ph.D. degrees from the University of Padova, Italy, in 2006, 2009, and 2013, respectively, and the M.Sc. degree in telecommunications engineering from the Technical University of Denmark, Denmark, in 2009, as part of the T.I.M.E. double degree program. From 2013 to 2015, he was a Postdoctoral Research Fellow with the Ming-Hsieh Department of Electrical Engineering, University of Southern California, Los Angeles, CA, USA, and from 2016 to 2020, he was an Assistant Professor with the School of Electrical and Computer Engineering, Purdue University, West Lafayette, IN, USA. He is currently an Associate Professor with the School of Electrical, Computer and Energy Engineering, Arizona State University, Tempe, AZ, USA. His research interests include 5G wireless networks, millimeter-wave communications, stochastic optimization, decentralized and federated learning over wireless systems. He served as Associate Editor for the IEEE TRANSACTIONS ON WIRELESS COMMUNICATIONS from 2016 to 2021, and currently serves as Editor for the IEEE TRANSACTIONS ON COMMUNICATIONS. He was the Co-Chair for the Distributed Machine Learning and Fog Network workshop at IEEE INFOCOM 2021, 2023 and 2024, the Wireless Communications Symposium at IEEE GLOBECOM 2020, the IoT, M2M, Sensor Networks, and Ad-Hoc Networking track at IEEE VTC 2020, and the Cognitive Computing and Networking symposium at ICNC 2018. He was the Technical Area Chair for the Communication Systems track at Asilomar 2023. He received the NSF CAREER award in 2021, the IEEE Communication Theory Technical Committee (CTTC) Early Achievement Award in 2022, and the IEEE Communications Society William R. Bennett Prize in 2024.

# Supplemental Document

In this supplemental document, we provide the proof of Lemma 2 of the main manuscript. We also provide additional numerical evaluations showcasing the parameters' selection of NCOTA-DGD, as well as comparisons with state-of-the-art schemes.

## PROOF OF LEMMA 2

In this section, we provide the proof of Lemma 2, restated below for ease of reference.

**Lemma 2.** Consider channels satisfying Assumption 1. Assume that the resource units are evenly allocated among  $m = 1, \dots, M$ , i.e.,  $|R_m - Q/M| < 1, \forall m$  (e.g., Fig. 2). Let:

$$\vartheta \triangleq \max_{i,j \neq i} \frac{1}{\Lambda_{ij}} \left( \frac{1}{Q} \sum_{q=1}^Q \mathbb{E}[ (|\mathbf{h}_{ij}|_q|^2 - \Lambda_{ij})^2 ] \right)^{1/2}, \quad (60)$$

$$\varpi \triangleq \max_{i,j \neq i} \frac{1}{\Lambda_{ij}} \left( \frac{1}{M} \sum_{m=1}^M \mathbb{E}[ (\hat{\lambda}_{ij}^{(m)} - \Lambda_{ij})^2 ] \right)^{1/2}, \quad (61)$$

$$\Lambda^* \triangleq \max_i \sum_{j \neq i} \Lambda_{ij}, \quad (62)$$

where  $\hat{\lambda}_{ij}^{(m)} = \frac{1}{R_m} \sum_{q \in \mathcal{R}_m} |\mathbf{h}_{ij}|_q|^2$  is the sample average channel gain across the resource units in the set  $\mathcal{R}_m$ . Then,  $\frac{1}{N} \sum_{i=1}^N \text{var}(\tilde{\mathbf{d}}_i) \leq \Sigma^{(1)} \triangleq \max_{\mathbf{z}, \mathbf{z}' \in \mathcal{Z}} \|\mathbf{z} - \mathbf{z}'\|^2$

$\times \frac{1}{1-p_{\text{tx}}} \left[ \frac{\sqrt{M}}{\sqrt{Q}} \sqrt{2(1+2\vartheta^2)} \Lambda^* + \frac{\sqrt{1+\varpi^2}}{\sqrt{p_{\text{tx}}}} \Lambda^* + \frac{\sqrt{M}}{\sqrt{Q}} \frac{N_0}{E p_{\text{tx}}} \right]^2$ . The value of the transmission probability  $p_{\text{tx}}$  minimizing this bound is the unique solution in  $(0, 1)$  of  $\sqrt{2(1+2\vartheta^2)} p_{\text{tx}}^{3/2} + \frac{\sqrt{Q}}{\sqrt{M}} \sqrt{1+\varpi^2} (2p_{\text{tx}}-1) + \frac{N_0}{\Lambda^* E} \frac{3p_{\text{tx}}-2}{\sqrt{p_{\text{tx}}}} = 0$ .

*Proof.* We start with

$$\frac{1}{N} \sum_{i=1}^N \text{var}(\tilde{\mathbf{d}}_i) \leq \max_i \text{var}(\tilde{\mathbf{d}}_i) = \max_i (\text{sdv}(\tilde{\mathbf{d}}_i))^2. \quad (63)$$

Hence, we focus on bounding  $\text{sdv}(\tilde{\mathbf{d}}_i)$  for a generic  $i$ . Using (12), we can express

$$\tilde{\mathbf{d}}_i - \mathbb{E}[\tilde{\mathbf{d}}_i] = \sum_{m=1}^M (r_{im} - \mathbb{E}[r_{im}])(\mathbf{z}_m - \mathbf{w}_i).$$

Next, we use Minkowski inequality [52, Lemma 14.10],  $\sqrt{\mathbb{E}[\|\sum_m \mathbf{a}_m\|^2]} \leq \sum_m \sqrt{\mathbb{E}[\|\mathbf{a}_m\|^2]}$ . It yields

$$\begin{aligned} \text{sdv}(\tilde{\mathbf{d}}_i) &= \sqrt{\mathbb{E}[\|\tilde{\mathbf{d}}_i - \mathbb{E}[\tilde{\mathbf{d}}_i]\|^2]} \\ &\leq \sum_{m=1}^M \text{sdv}(r_{im}) \|\mathbf{z}_m - \mathbf{w}_i\|. \end{aligned} \quad (64)$$

We bound  $\|\mathbf{z}_m - \mathbf{w}_i\|$  by using the fact that  $\mathbf{w}_i = \sum_{m'=1}^M [\mathbf{p}_i]_{m'} \mathbf{z}_{m'}$  and the triangle inequality, yielding

$$\|\mathbf{z}_m - \mathbf{w}_i\| \leq \sum_{m'=1}^M [\mathbf{p}_i]_{m'} \|\mathbf{z}_m - \mathbf{z}_{m'}\|$$

$$\leq \max_{m', m''} \|\mathbf{z}_{m''} - \mathbf{z}_{m'}\| = \max_{\mathbf{z}, \mathbf{z}' \in \mathcal{Z}} \|\mathbf{z} - \mathbf{z}'\|,$$

so that (64) is further upper bounded as

$$\text{sdv}(\tilde{\mathbf{d}}_i) \leq \max_{\mathbf{z}, \mathbf{z}' \in \mathcal{Z}} \|\mathbf{z} - \mathbf{z}'\| \sum_{m=1}^M \text{sdv}(r_{im}). \quad (65)$$

We now focus on bounding  $\text{sdv}(r_{im}) = \sqrt{\text{var}(r_{im})}$ . We use  $\text{var}(X) = \mathbb{E}_A[\text{var}(X|A)] + \text{var}(\mathbb{E}[X|A])$  to express

$$\text{var}(r_{im}) = \mathbb{E} \left[ \text{var} \left( r_{im} \mid \varsigma, \chi_{-i}, \chi_i, \mathbf{h} \right) \right] \quad (66)$$

$$+ \text{var} \left( \mathbb{E}[r_{im} \mid \varsigma, \chi_{-i}, \chi_i, \mathbf{h}] \right). \quad (67)$$

The first variance term captures the impact of the AWGN noise and random phase injected at the transmitters; the second term captures the impact of the randomness in the channels ( $\mathbf{h}$ ), circular shift ( $\varsigma$ ), random transmission of node  $i$  ( $\chi_i$ ) and of all other nodes ( $\chi_{-i}$ ). Next, we bound each variance term individually.

Bounding  $\mathbb{E}[\text{var}(r_{im} \mid \varsigma, \chi_{-i}, \chi_i, \mathbf{h})]$ : Let  $m' \triangleq m \oplus \varsigma$  and

$$\begin{aligned} A_q &\triangleq \sum_{j \neq i} \chi_j [\mathbf{h}_{ij}]_q [\mathbf{x}_j]_q \\ &= \sqrt{\frac{EQ}{R_{m'}}} \sum_{j \neq i} \chi_j e^{j[\theta_j]_q} [\mathbf{h}_{ij}]_q \sqrt{[\mathbf{p}_j]_m}, \quad \forall q \in \mathcal{R}_{m'}. \end{aligned}$$

Then, we can express  $[\mathbf{y}_i]_q = A_q + [\mathbf{n}_i]_q$  and

$$r_{im} = \frac{1 - \chi_i}{EQ p_{\text{tx}} (1 - p_{\text{tx}})} \sum_{q \in \mathcal{R}_{m'}} (|A_q + [\mathbf{n}_i]_q|^2 - N_0).$$

Note that, when conditioned on  $\varsigma, \chi_{-i}, \chi_i, \mathbf{h}$  (hence on  $m'$ ), the terms  $|A_q + [\mathbf{n}_i]_q|^2$  are independent across  $q$ , due to independence of  $[\mathbf{n}_i]_q$ , and of the phases  $[\theta_j]_q$  across  $q \in \mathcal{R}_{m'}$  and  $j$ . Therefore,

$$\begin{aligned} \text{var}(r_{im} \mid \varsigma, \chi_{-i}, \chi_i, \mathbf{h}) &= \frac{1 - \chi_i}{E^2 Q^2 p_{\text{tx}}^2 (1 - p_{\text{tx}})^2} \quad (68) \\ &\times \sum_{q \in \mathcal{R}_{m'}} \text{var}(|A_q + [\mathbf{n}_i]_q|^2 \mid \varsigma, \chi_{-i}, \mathbf{h}). \end{aligned}$$

Using the independence of the noise and of the phases injected at the transmitters (across transmitters  $j$ ), the fact that  $\mathbb{E}[e^{j[\theta_{j_1} - \theta_{j_2} + \theta_{j_3} - \theta_{j_4}]_q}] = \mathbb{1}[j_3 = j_4, j_1 = j_2] + \mathbb{1}[j_3 = j_2, j_4 = j_1, j_1 \neq j_2]$ , and  $\mathbb{E}[|\mathbf{n}_i]_q|^4] = 2N_0^2$ , we find that

$$\begin{aligned} \text{var}(|A_q + [\mathbf{n}_i]_q|^2 \mid \varsigma, \chi_{-i}, \mathbf{h}) &= \frac{EQ}{R_{m'}} \sum_{j \neq i} \chi_j |\mathbf{h}_{ij}|_q^2 [\mathbf{p}_j]_m \\ &\times \left( \frac{EQ}{R_{m'}} \sum_{j' \neq i, j} \chi_{j'} |\mathbf{h}_{ij'}|_q^2 [\mathbf{p}_{j'}]_m + 2N_0 \right) + N_0^2. \end{aligned}$$

Next, we compute the expectation of this variance term with respect to the random transmissions of nodes  $j \neq i$ . Since these are independent across  $j \neq j'$  and occur with probability



$p_{\text{tx}}$ , we obtain

$$\begin{aligned} & \mathbb{E}_{\chi_{-i}}[\text{var}(|A_q + [\mathbf{n}_i]_q|^2 | \varsigma, \chi_{-i}, \mathbf{h})] \\ &= \left( \frac{EQp_{\text{tx}}}{R_{m'}} \sum_{j \neq i} |[\mathbf{h}_{ij}]_q|^2 [\mathbf{p}_j]_m + N_0 \right)^2 \\ & \quad - \frac{(EQp_{\text{tx}})^2}{(R_{m'})^2} \sum_{j \neq i} |[\mathbf{h}_{ij}]_q|^4 [\mathbf{p}_j]_m^2. \end{aligned}$$

Substituting in the expression of  $\text{var}(r_{im} | \varsigma, \chi_{-i}, \chi_i, \mathbf{h})$  in (68), discarding the negative term above, and further taking the expectation with respect to the transmission indicator  $\chi_i \in \{0, 1\}$ , the circular shift  $\varsigma$  (hence  $m' = m \oplus \varsigma$  becomes uniform in  $\{1, \dots, M\}$ ), and the channels, yields

$$\begin{aligned} \mathbb{E}[\text{var}(r_{im} | \varsigma, \chi_{-i}, \chi_i, \mathbf{h})] &= \frac{1}{E^2 Q^2 p_{\text{tx}}^2 (1 - p_{\text{tx}})} \\ & \times \frac{1}{M} \sum_{m', q} \mathbb{E}_{\mathbf{h}} \left[ \left( \frac{EQp_{\text{tx}}}{R_{m'}} \sum_{j \neq i} |[\mathbf{h}_{ij}]_q|^2 [\mathbf{p}_j]_m + N_0 \right)^2 \right], \quad (69) \end{aligned}$$

where we defined the shorthand notation  $\sum_{m', q} \equiv \sum_{m'=1}^M \sum_{q \in \mathcal{R}_{m'}}$ . The term above takes the form

$$\sum_t \mathbb{E}[(\sum_j \alpha_{jt})^2]$$

for suitable  $\alpha_{jt}$ . We can upper bound it as

$$\begin{aligned} &= \sum_{j', j} \sum_t \mathbb{E}[\alpha_{jt} \alpha_{j't}] \leq \sum_{j', j} \sum_t \sqrt{\mathbb{E}[\alpha_{jt}^2]} \sqrt{\mathbb{E}[\alpha_{j't}^2]} \\ &\leq \sum_{j', j} \sqrt{\sum_t \mathbb{E}[\alpha_{jt}^2]} \sqrt{\sum_t \mathbb{E}[\alpha_{j't}^2]} = \left( \sum_j \sqrt{\sum_t \mathbb{E}[\alpha_{jt}^2]} \right)^2, \end{aligned}$$

where in the first step we used Holder's inequality, in the second step we used Cauchy-Schwarz inequality. Using this bound in (69) yields

$$\begin{aligned} & \mathbb{E}[\text{var}(r_{im} | \varsigma, \mathcal{T}_{-i}, \tau_i, \mathbf{h})] \\ &\leq \frac{1}{1 - p_{\text{tx}}} \left( \sum_{j \neq i} \sqrt{\sum_{m', q} \frac{1}{MR_{m'}^2} \mathbb{E}[|[\mathbf{h}_{ij}]_q|^4] [\mathbf{p}_j]_m} \right. \\ & \quad \left. + \frac{N_0}{\sqrt{MQE} p_{\text{tx}}} \right)^2. \quad (70) \end{aligned}$$

We further bound

$$\begin{aligned} & \sum_{m', q} \frac{1}{MR_{m'}^2} \mathbb{E}[|[\mathbf{h}_{ij}]_q|^4] \leq \frac{2M}{Q} \sum_{m', q} \frac{1}{MR_{m'}} \mathbb{E}[|[\mathbf{h}_{ij}]_q|^4] \\ &= \frac{2M}{Q} \left( \sum_{m'=1}^M \sum_{q \in \mathcal{R}_{m'}} \frac{1}{MR_{m'}} \mathbb{E}[ (|[\mathbf{h}_{ij}]_q|^2 - \Lambda_{ij})^2 ] + \Lambda_{ij}^2 \right) \\ &\leq \frac{2M}{Q} \left( \frac{2}{Q} \sum_{q=1}^Q \mathbb{E}[ (|[\mathbf{h}_{ij}]_q|^2 - \Lambda_{ij})^2 ] + \Lambda_{ij}^2 \right) \\ &\leq \frac{2M}{Q} (1 + 2\vartheta^2) \Lambda_{ij}^2, \end{aligned}$$

where in the first and third steps we used  $1/R_{m'} \leq 2M/Q$  (a consequence of the uniform allocation of resource units), in

the second step we used the fact that (Assumption 1)

$$\frac{1}{R_{m'}} \sum_{q \in \mathcal{R}_{m'}} \mathbb{E}[|[\mathbf{h}_{ij}]_q|^2] = \Lambda_{ij}^{(m')}, \quad \Lambda_{ij} = \frac{1}{M} \sum_{m'=1}^M \Lambda_{ij}^{(m')},$$

and in the last step we used (60). Substituting this bound in (70) yields

$$\begin{aligned} & \mathbb{E}[\text{var}(r_{im} | \varsigma, \chi_{-i}, \chi_i, \mathbf{h})] \\ &\leq \frac{M}{Q(1 - p_{\text{tx}})} \left( \sqrt{2(1 + 2\vartheta^2)} \sum_{j \neq i} \Lambda_{ij} [\mathbf{p}_j]_m + \frac{N_0}{EMp_{\text{tx}}} \right)^2. \end{aligned}$$

Bounding  $\text{var}(\mathbb{E}[r_{im} | \varsigma, \chi_{-i}, \chi_i, \mathbf{h}])$ : Note that

$$\text{var}(\mathbb{E}[r_{im} | \varsigma, \chi_{-i}, \chi_i, \mathbf{h}]) \leq \mathbb{E}[\mathbb{E}[r_{im} | \varsigma, \chi_{-i}, \chi_i, \mathbf{h}]^2]. \quad (71)$$

From (20) and (7),

$$\mathbb{E}[r_{im} | \varsigma, \chi_{-i}, \chi_i, \mathbf{h}] = (1 - \chi_i) \frac{\sum_{j \neq i} \chi_j \hat{\lambda}_{ij}^{(m')} [\mathbf{p}_j]_m}{p_{\text{tx}} (1 - p_{\text{tx}})} \quad (72)$$

where  $\hat{\lambda}_{ij}^{(m')} = \frac{1}{R_{m'}} \sum_{q \in \mathcal{R}_{m'}} |[\mathbf{h}_{ij}]_q|^2$  is the sample average gain across the resource units in the set  $\mathcal{R}_{m'}$ . We square and take the expectation with respect to  $(\varsigma, \chi_{-i}, \chi_i, \mathbf{h})$ , yielding

$$\begin{aligned} \mathbb{E}[\mathbb{E}[r_{im} | \varsigma, \chi_{-i}, \chi_i, \mathbf{h}]^2] &= \frac{\mathbb{E}[(\sum_{j \neq i} \chi_j \hat{\lambda}_{ij}^{(m')} [\mathbf{p}_j]_m)^2]}{p_{\text{tx}}^2 (1 - p_{\text{tx}})} \\ &\leq \frac{\left( \sum_{j \neq i} \sqrt{\mathbb{E}[\chi_j (\hat{\lambda}_{ij}^{(m')})^2]} [\mathbf{p}_j]_m \right)^2}{p_{\text{tx}}^2 (1 - p_{\text{tx}})} \quad (73) \end{aligned}$$

where in the last step we used Holder's inequality  $\mathbb{E}[AB] = \sqrt{\mathbb{E}[A^2]} \sqrt{\mathbb{E}[B^2]}$  with the random variables  $A = \chi_j \hat{\lambda}_{ij}^{(m')}$  and  $B = \chi_{j'} \hat{\lambda}_{ij'}^{(m')}$ . Furthermore,

$$\mathbb{E}[\chi_j (\hat{\lambda}_{ij}^{(m')})^2] = \frac{p_{\text{tx}}}{M} \sum_{m'=1}^M \mathbb{E}[(\hat{\lambda}_{ij}^{(m')})^2],$$

where we computed the expectation with respect to the transmission indicator and the circular shift  $\varsigma$  (hence  $m' = m \oplus \varsigma$  uniform in  $\{1, \dots, M\}$ ). We continue as

$$\begin{aligned} \mathbb{E}[\chi_j (\hat{\lambda}_{ij}^{(m')})^2] &= p_{\text{tx}} \left( \frac{1}{M} \sum_{m'=1}^M \mathbb{E}[(\hat{\lambda}_{ij}^{(m')} - \Lambda_{ij})^2] + \Lambda_{ij}^2 \right) \\ &\leq p_{\text{tx}} (1 + \varpi^2) \Lambda_{ij}^2, \end{aligned}$$

where we used the fact that  $\frac{1}{M} \mathbb{E}[\hat{\lambda}_{ij}^{(m')}] = \Lambda_{ij}^{(m')}$  and  $\Lambda_{ij} = \frac{1}{M} \sum_{m'=1}^M \Lambda_{ij}^{(m')}$ , followed by (61). Substituting this bound into (73) and then in (71) yields

$$\mathbb{E}[\text{var}(r_{im} | \varsigma, \mathcal{T}_{-i}, \tau_i, \mathbf{h})] \leq \frac{1 + \varpi^2}{p_{\text{tx}} (1 - p_{\text{tx}})} \left( \sum_{j \neq i} \Lambda_{ij} [\mathbf{p}_j]_m \right)^2.$$

Final results: Combining the results together into (66) yields

$$\begin{aligned} \text{var}(r_{im}) &\leq \frac{1 + \varpi^2}{p_{\text{tx}} (1 - p_{\text{tx}})} \left( \sum_{j \neq i} \Lambda_{ij} [\mathbf{p}_j]_m \right)^2 \\ & \quad + \frac{M}{Q(1 - p_{\text{tx}})} \left( \sqrt{2(1 + 2\vartheta^2)} \sum_{j \neq i} \Lambda_{ij} [\mathbf{p}_j]_m + \frac{N_0}{EMp_{\text{tx}}} \right)^2. \end{aligned}$$

Finally, we take the square root of both sides, along with

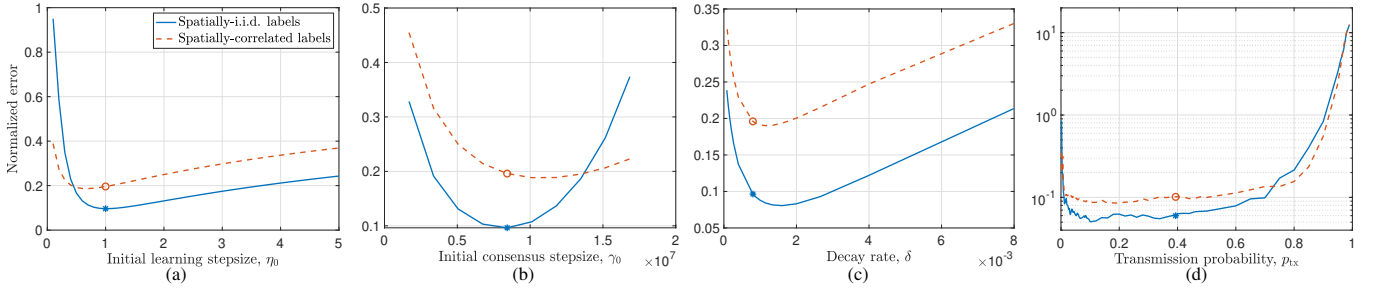


Fig. 6: Normalized error vs initial learning stepsize (a), initial consensus stepsize (b), decay rate  $\delta$  (c), and transmission probability  $p_{\text{tx}}$  (d), evaluated after 2000ms of execution time, under spatially-i.i.d. (solid lines) and -dependent (dashed lines) scenarios, with i.i.d. channels over frames. The markers denote the *Baseline* configuration, adopted in Sec. V:  $\eta_0 = \frac{2}{\mu+L}$ ,  $\gamma_0 = \frac{0.05}{\rho^2}$ ,  $\delta = \frac{4}{5}\mu\eta_0$ ,  $p_{\text{tx}}$  as in Lemma 2. The common legend is shown in figure (a).

$\sqrt{\sum_{\ell} a_{\ell}^2} \leq \sum_{\ell} a_{\ell}$  for  $a_i \geq 0$ , add over  $m$  and use the fact that  $\sum_m [\mathbf{p}_j]_m = 1$ . These steps yield

$$\begin{aligned} \sum_{m=1}^M \text{sdv}(r_{im}) &\leq \frac{\sqrt{M}}{\sqrt{Q}\sqrt{1-p_{\text{tx}}}} \sqrt{2(1+2\vartheta^2)} \sum_{j \neq i} \Lambda_{ij} \\ &+ \frac{\sqrt{M}}{\sqrt{Q}\sqrt{1-p_{\text{tx}}}} \frac{N_0}{E p_{\text{tx}}} + \frac{\sqrt{1+\varpi^2}}{\sqrt{p_{\text{tx}}}\sqrt{1-p_{\text{tx}}}} \sum_{j \neq i} \Lambda_{ij} \triangleq g(p_{\text{tx}}). \end{aligned}$$

The final result is obtained by using the previous bound in (65), along with  $\sum_{j \neq i} \Lambda_{ij} \leq \Lambda^*$  (see (62)). Finally, it is straightforward to show that  $\lim_{p_{\text{tx}} \rightarrow 0} g(p_{\text{tx}}) = \infty$ ,  $\lim_{p_{\text{tx}} \rightarrow 1} g(p_{\text{tx}}) = \infty$ , and

$$g'(p_{\text{tx}}) \propto A p_{\text{tx}}^{3/2} + B(2p_{\text{tx}} - 1) + C \frac{3p_{\text{tx}} - 2}{\sqrt{p_{\text{tx}}}} \triangleq h(p_{\text{tx}})$$

where  $A = \frac{\sqrt{M}}{\sqrt{Q}} \sqrt{2(1+2\vartheta^2)}$ ,  $B = \sqrt{1+\varpi^2}$ ,  $C = \frac{\sqrt{M}}{\sqrt{Q}} \frac{N_0}{\Lambda^* E}$ . The function  $h(p_{\text{tx}})$  is decreasing in  $p_{\text{tx}}$  (with  $\lim_{p_{\text{tx}} \rightarrow 0} h(p_{\text{tx}}) = -\infty$ ,  $h(1) = A+B+C$ , hence there exists a unique  $p_{\text{tx}}^* \in (0, 1)$  such that  $h(p_{\text{tx}}^*) = 0$ , hence  $g'(p_{\text{tx}}^*) = 0$ . Such  $p_{\text{tx}}^*$  minimizes  $g(p_{\text{tx}})$ , hence the upper bound  $\Sigma^{(1)}$  on  $\frac{1}{N} \sum_{i=1}^N \text{var}(\hat{\mathbf{d}}_i)$ .  $\square$

#### PERFORMANCE OF NCOTA-DGD WITH RESPECT TO STEPSIZE PARAMETERS AND TRANSMISSION PROBABILITY

In this section, we provide additional numerical evaluations to Sec. V. The simulation parameters and algorithm descriptions are provided in Sec. V.

We evaluate the performance of NCOTA-DGD in terms of its normalized error after 2000ms of execution time, for a network with  $N = 200$  nodes. We use the CP0 codebook of Example 1 with  $M=2d+1=901$  codewords, requiring two OFDM symbols ( $Q=1024$ ), and yielding a frame of duration  $T=2T_{\text{ofdm}}=258\mu\text{s}$ . It follows Algorithm 1.

In Fig. 6, we plot the normalized error versus some key parameters of NCOTA-DGD: the initial learning stepsize  $\eta_0$  (a), the initial consensus stepsize  $\gamma_0$  (b), the decay rate  $\delta$  (c), and the transmission probability  $p_{\text{tx}}$  (d). To this end, we vary one such parameter, while setting the other parameters equal to the *Baseline* configuration. The latter adopts  $\eta_0 = \frac{2}{\mu+L}$ ,  $\gamma_0 = \frac{0.05}{\rho^2}$ ,  $\delta = \frac{4}{5}\mu\eta_0$ ,  $p_{\text{tx}}$  as in Lemma 2. For instance, Fig. 6.a is obtained by varying  $\eta_0$ , while setting the  $\gamma_0$ ,  $\delta$  and  $p_{\text{tx}}$  parameters as their baseline values.

In Fig. 6.a, we plot the normalized error versus the initial learning stepsize  $\eta_0$ . As expected, tuning of  $\eta_0$  regulates the magnitude of gradient steps, hence the learning progress. A

smaller  $\eta_0$  slows down the progress of the algorithm, resulting in slower convergence and higher normalized error. On the other hand, if the stepsize is too large, the optimization algorithm might oscillate around the minimizer or even diverge away from it. Note that the baseline value  $\eta_0 = \frac{2}{\mu+L}$  (denoted with markers) is the maximum stepsize that guarantees convergence of gradient descent, for the class of strongly-convex and smooth loss functions.

In Fig. 6.b, we plot the normalized error versus the initial consensus stepsize  $\gamma_0$ . As explained in the discussion following Theorem 4, tuning  $\gamma_0$  reflects a delicate balance between speeding up information propagation (favored by larger  $\gamma_0$ ) and minimizing error propagation (smaller  $\gamma_0$ ). This trade-off is in line with the behavior observed in the figure.

In Fig. 6.c, we plot the normalized error versus the decay rate  $\delta$ . As explained in the discussion following Theorem 4, the choice  $\delta = \frac{4}{5}\mu\eta_0$  is the one that minimizes the convergence bounds stated in Theorem 4, hence the value  $\delta = \frac{4}{5}\mu\eta_0$  is employed in the numerical evaluations of Sec. V. Remarkably, the plots of 6.c demonstrate the same monotonic behavior expected from Theorem 4 in the regime  $\delta \leq \frac{4}{5}\mu\eta_0$ . They also demonstrate that, if the condition  $\delta \leq \frac{4}{5}\mu\eta_0$  of Theorem 4 is violated, the normalized error quickly diverges. In this regime, the stepsizes decrease too quickly, preventing the algorithm from making a tangible progress. This numerical evaluation further motivates the use of decreasing vs constant ( $\delta \rightarrow 0$ ) stepsizes developed in this paper.

In Fig. 6.d, we plot the normalized error versus the transmission probability  $p_{\text{tx}}$ . We remind that the baseline value shown with markers is the one given by Lemma 2 and used in the numerical evaluations of Sec. V. This value minimizes the upper bound on the variance of the disagreement signal estimate, given in Lemma 2. Indeed, Fig. 6.d confirms that the optimal  $p_{\text{tx}}$  value found via Lemma 2 attains nearly optimal numerical performance. Furthermore, the normalized error exhibits a mild dependence with respect to  $p_{\text{tx}}$  around such optimal value (in the interval  $[0.1, 0.5]$ ), and quickly diverges as  $p_{\text{tx}} \rightarrow 0$  (the transmissions are too sporadic) or  $p_{\text{tx}} \rightarrow 1$  (each node operates as a receiver too infrequently). This implies that precise knowledge of propagation parameters  $\vartheta$ ,  $\varpi$  and  $\Lambda^*$ , affecting the design of  $p_{\text{tx}}$ , is not critical.

#### ADDITIONAL COMPARISONS WITH STATE-OF-THE-ART SCHEMES

Fig. 7 depicts the performance of the state-of-the-art schemes implemented in Sec. V-B versus time, for the scenario

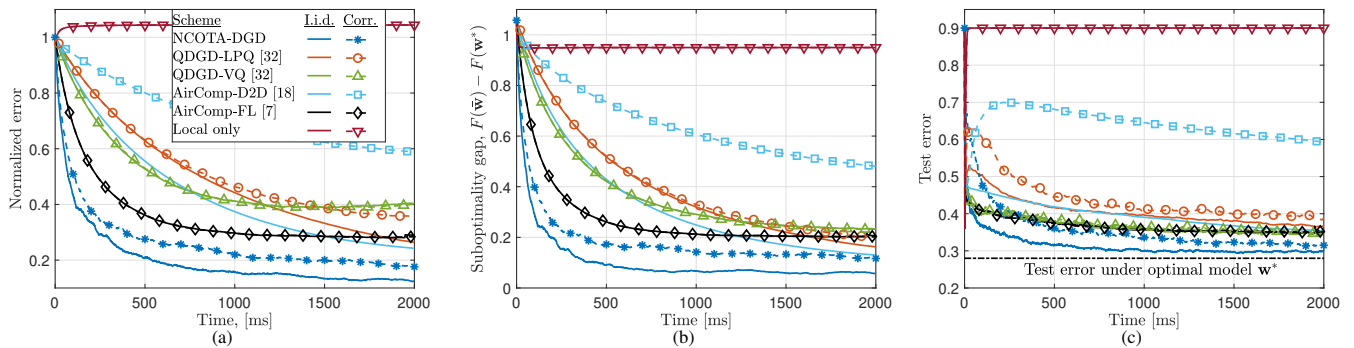


Fig. 7: Normalized error (a), suboptimality gap (b), test error (c) vs time, under both spatially-i.i.d. and -dependent label scenarios, with i.i.d. channels over frames. Common legend shown in figure (a).

with  $N = 200$  nodes, with i.i.d. channels over frames. We evaluated the performance under both spatially-i.i.d. (solid lines) and spatially-dependent (dashed with markers) label scenarios. As also noted in the comments of Fig. 5, smaller normalized error typically translates to smaller suboptimality gap and test error, and the performance generally degrades in the spatially-dependent scenario.

In both scenarios, we note that NCOTA-DGD achieves the best performance across time, followed by *AirComp-FL*.

The worst performance is attained by *Local only*, since each node optimizes its local function and does not exploit inter-agent communications. As noted in the comments of Sec. V-B, *AirComp-FL* benefits from its star-based topology: all communications happen to and from the parameter server, which maintains model synchronization across the network. However, this scheme also suffers from the same, due to the communication bottleneck experienced by the edge nodes, as discussed in Sec. V-B.